TU Delft

Delft University of Technology

Polygon-Informed Cross-Track Altimetry (PICTA)

Estimating river water level profiles with the Sentinel-6 altimeter

Ehlers, Frithjof; Slobbe, Cornelis; Schlembach, Florian; Kleinherenbrink, Marcel; Verlaan, Martin

DOI
10.1016/j.rse.2024.114479

Publication date
2024

Document Version
Final published version

Published in
Remote Sensing of Environment

Citation (APA)
Ehlers, F., Slobbe, C., Schlembach, F., Kleinherenbrink, M., & Verlaan, M. (2024). Polygon-Informed Cross-Track Altimetry (PICTA): Estimating river water level profiles with the Sentinel-6 altimeter. *Remote Sensing of Environment*, *316*, Article 114479. https://doi.org/10.1016/j.rse.2024.114479

Important note
To cite this publication, please use the final published version (if applicable).
Please check the document version above.

Copyright
Other than for strictly personal use, it is not permitted to download, forward or distribute the text or part of it, without the consent of the author(s) and/or copyright holder(s), unless the work is under an open content license such as Creative Commons.

Takedown policy
Please contact us and provide details if you believe this document breaches copyrights.
We will remove access to the work immediately and investigate your claim.

This work is downloaded from Delft University of Technology.
For technical reasons the number of authors shown on this cover page is limited to a maximum of 10.

Remote Sensing of Environment 316 (2025) 114479

Contents lists available at ScienceDirect

Remote Sensing of Environment

journal homepage: www.elsevier.com/locate/rse

Polygon-Informed Cross-Track Altimetry (PICTA): Estimating river water level profiles with the Sentinel-6 altimeter

Frithjof Ehlers [a,*], Cornelis Slobbe [a], Florian Schlembach [b], Marcel Kleinherenbrink [a,c], Martin Verlaan [d,e]

[a] Geoscience & Remote Sensing, Delft University of Technology (TU Delft), Stevinweg 1, Delft, 2628 CN, South Holland, Netherlands
[b] Deutsches Geodätisches Forschungsinstitut, Technical University of Munich (DGFI-TUM), Alfons-Goppel-Straße 11, Munich, 80539, Bavaria, Germany
[c] European Space Research and Technology Centre (ESA, ESTEC), Keplerlaan 1, Noordwijk, 2201 AZ, South Holland, Netherlands
[d] Mathematical Physics, Delft University of Technology (TU Delft), Mekelweg 4, Delft, 2628 CD, South Holland, Netherlands
[e] Deltares, Boussinesqweg 1, Delft, 2629 HV, South Holland, Netherlands

ARTICLE INFO

Edited by Menghua Wang

Dataset link: https://doi.org/10.4121/304db898-f99c-490a-97c4-13f919ae3c05, https://github.com/fehlers94/Polygon-informed-cross-track-altimetry-PICTA/tree/v1.0, https://doi.org/10.5281/zenodo.13165945

Keywords:
Satellite altimetry
Radar altimeter
Sentinel-6
River water levels
Water Surface Elevation
Rivers
Hydrology
Inland Waters
River slope
Water level profiles
Swath
Fully focused SAR
FF-SAR
PICTA
SAR
SWOT

ABSTRACT

Traditionally, nadir-looking satellite radar altimeters provide water levels of rivers only at intersections with the satellite's ground track, called virtual stations. These observations have limited spatial coverage because such cross-overs are sparse, depending on the altimeter's orbit. In this work, we introduce the novel concept of Polygon-Informed Cross-Track Altimetry (PICTA), enabling accurate estimation of water levels at cross-track distances — for as long as the target's signal is recorded in the altimeter's range window. Using fully-focused SAR data from the Sentinel-6 altimetry mission, we demonstrate how the new approach can provide detailed river water level profiles over a ground swath of about 14 km cross-track width and with an along-track resolution as fine as 10 m. On the one hand, this marks a drastic improvement in the number of available measurements when compared to the virtual station approach, on the other hand, for the first time, water surface slopes and level variations along the river, caused by rapids, dams, and sluices, can be directly observed using a nadir radar altimeter. The validation over two river segments in France reveals biases as low as ±4 cm and random errors on the order of 3–8 cm at 30 m along-track resolution. The new PICTA concept can potentially be generalized to other targets, such as lakes or even coastlines.

1. Introduction

Nadir-looking satellite radar altimeters typically provide one-dimensional measurements of water surface elevation, meaning that they deliver measurements only along the line of their ground-track. In this notion, particularly rivers are only measured at a few locations where the ground track and the river meet (e.g., Birkett, 1998; Alsdorf and Lettenmaier, 2003; Crétaux et al., 2016), called virtual stations (databases including such measurements are described in Copernicus, 2024; Crétaux et al., 2011; Calmant et al., 2013; Schwatke et al., 2015; Birkett et al., 2011; Gustafsson et al., 2018).

This limitation can be overcome with the help of Synthetic Aperture Radar (SAR) interferometry and a slightly side-looking geometry, as demonstrated by the Surface Water and Ocean Topography (SWOT) satellite mission (Biancamaria et al., 2016; Fu et al., 2024), which delivers two-dimensional water surface elevation maps within its ground swath. However, to improve global river discharge estimates, which is

* Corresponding author.
E-mail address: f.ehlers@tudelft.nl (F. Ehlers).

https://doi.org/10.1016/j.rse.2024.114479
Received 30 May 2024; Received in revised form 15 October 2024; Accepted 17 October 2024
Available online 1 November 2024
0034-4257/© 2024 The Authors. Published by Elsevier Inc. This is an open access article under the CC BY license (http://creativecommons.org/licenses/by/4.0/).

one of SWOT's main mission objectives, these maps need to be post-processed to obtain accurate one-dimensional longitudinal profiles of river water level, slope and width (Durand et al., 2023). Since river water level profiles are also one-dimensional in practice, and since the SWOT mission is designed for a limited lifetime and temporal sampling, one may wonder whether an interferometric system is always strictly necessary to provide the desired information.

Indeed, Boy et al. (2023) and Daguzé et al. (2023) demonstrated recently that it is principally possible to obtain densely-sampled river water level profiles from fully-focused SAR (FFSAR) (Egido and Smith, 2017) data of the Sentinel-6 nadir-looking altimeter. In essence, the cross-track elevation measurements are feasible because the nadir radar altimeter footprint and the recorded range window extend several kilometers in cross-track direction, so that targets like rivers and lakes are still visible in the altimeter waveforms (for lakes see also Boy et al., 2022; Yanez et al., 2024). Slanted (off-nadir) range measurements to the river can then be combined with a known river center line to infer the river water level. Throughout this manuscript, we will refer to the entirety of such approaches as Polygon-Informed Cross-Track Altimetry (PICTA), since they require a-priori knowledge of the target's location in terms of a center line or contour. The PICTA method also requires very high along-track resolutions on the order of meters unless the river is very well aligned with the satellite ground track, as will be explained in Section 2. This resolution can only be guaranteed with an open-burst pulse sampling scheme of the radar altimeter (Donlon et al., 2021; Egido and Smith, 2017), which is currently only implemented by the Sentinel-6 mission. This implies that FFSAR data from the CryoSat −2 and Sentinel-3 missions are less well-suited, because the signal of a single scatterer is still spread out over approximately 300 m along the ground track due to strong ambiguities (grating lobes of the point target response) (Ehlers et al., 2022, compare Figs. 4 and 6).

The advantages of the PICTA approach are manifold. On one hand, PICTA enables the direct measurement of entire river water level profiles and the computation of local water surface slopes from just a single SAR altimeter overpass, while previously, river water level profiles and the water surface slopes could only be interpolated by utilizing multi-mission altimetry processing approaches (for a non-extensive overview see Schwatke et al., 2023; Birkinshaw et al., 2014; Tourian et al., 2016; Boergens et al., 2017; Tourian et al., 2017; Nielsen et al., 2022, and references therein). PICTA data from Sentinel-6 complements the recently launched SWOT mission regarding temporal coverage and regarding mission lifetime. Firstly, SWOT provides a global median of two measurements per cycle of 21 days (Altenau et al., 2021), which is often too few to capture extreme events (Belloni et al., 2021, and references therein). Considering Sentinel-6's orbit repeat cycle of 10 days, the temporal sampling rate may be doubled over areas covered by the mission's altimeter footprint. Secondly, Sentinel missions are designed for data continuity, while SWOT's planned mission lifetime is 3 years. Considering also the launch dates of the SWOT and Sentinel-6 A satellites, December 2022 and November 2020, respectively, the Sentinel-6 mission has already two full years of additional data to offer. Finally, since the water level measurements from SWOT and Sentinel-6 are obtained with different instruments and via different methods, their error budget differs as well: SWOT observations may show systematic height errors between 3–6 cm over inland caused by, e.g., remaining uncertainties in baseline roll angle and baseline length (Dibarboure et al., 2022, 2012), which is not the case for Sentinel-6. A comparison between the two measurements therefore offers great potential for cross-calibration.

However, Boy et al. (2023) imposed very strong conditions on feasible scenarios for PICTA, because of a worsened error budget on the one hand and several unsolved challenges in the data processing on the other, including signal folding, river bifurcations, river meanders and elevation discontinuities at dams and sluices. Both the approaches of Boy et al. (2023) and Daguzé et al. (2023) make use of a river center line instead of a polygon, such as applied in this work, leading to a worsened error budget of their methods. Therefore, Boy et al. (2023) concludes that a water level error requirement of less than 15 cm limits the method's applicability to rivers with less than 200 m width and cross-track distances smaller than 2 km. We will demonstrate here that the errors may be less than 10 cm up to cross-track distance of 5–7 km when using a river polygon. Furthermore, the approaches of Boy et al. (2023) and Daguzé et al. (2023) assume the river's echoes to closely resemble a sinc^2-function. In fact, the echoes at increased river widths or cross-track distances will no more fulfill this assumption, as they are significantly widened due to the geometry. This will lead us to apply an alternative retracking strategy in this work. One of the primary open challenges, however, lies in automatically and reliably associating each range signal with its corresponding ground target, as discussed by Daguzé et al. (2023), so to correctly calculate elevation. Achieving this alignment is critical, as it ensures the accuracy of the obtained river water level data. Up to this date, although PICTA was demonstrated by Boy et al. (2023), no PICTA algorithm is documented in scientific literature, and the error budget and working principle of PICTA have never before been thoroughly discussed.

In this manuscript, we take up this challenge and develop and validate here the first semi-automated PICTA algorithm to routinely extract longitudinal river water level profiles from data of the Sentinel-6 altimeter, using FFSAR processing (Egido and Smith, 2017; Guccione et al., 2018; Kleinherenbrink et al., 2020a; Ehlers et al., 2022) in combination with a-priori river polygons. It is the first algorithm of its kind that can yield direct measurements of river water level profiles from a nadir-looking altimeter despite the afore-mentioned challenges. The manuscript is organized as follows. First, Section 2 outlines in detail the measurement principle, our PICTA algorithm for river level retrieval, and the extended error budget of PICTA as compared to nadir altimetry. The remainder of the manuscript is then reserved for the demonstration and validation of the algorithm. First, an overview of the case studies and all the data used throughout this work is provided in Section 3, whereafter the performance of the PICTA processing is assessed in two case studies in France throughout Section 4, using in-situ and airborne data for validation. Section 5 discusses the remaining challenges and limitations of the technique, after which we conclude in Section 6. Note that the term river water level will be used synonymously to the common term of Water Surface Elevation (WSE) throughout this manuscript, because the work is concerned with rivers specifically.

2. Methods

2.1. Measurement principle

In order to outline the measurement principle behind the river water level profile extraction, it is first necessary to briefly discuss the altimeter river return signals. The processed altimeter return signal can be plotted as an image of power over range and along-track distance, see Fig. 1B-D. A single row of this signal, namely power over range, is called a waveform, while the whole image will be called radargram throughout this work.

The Sentinel-6 altimeter data can be processed in different ways (EUMETSAT, 2021), which yields radargrams with very different along-track resolution according to the chosen aperture within the SAR-focusing. We distinguish here between (i) the Low Resolution Mode (LRM) (EUMETSAT, 2021), in which no coherent processing/SAR-focusing is applied, (ii) the Delay-Doppler or SAR mode (Raney, 1998, 2012; EUMETSAT, 2021) in which SAR-focusing is performed over individual bursts of 64 pulses and (iii) the fully-focused SAR (FFSAR) mode (Egido and Smith, 2017) using a long synthetic aperture of 2.2 s for SAR-focusing in this particular case. The range resolution of all radargrams is identical, but the along-track resolution differs greatly. For LRM it is comparable to the size of the antenna footprint on the order of several kilometers, while the theoretical along-track resolution in SAR mode and FFSAR mode are approximately 300 m and 1 m,

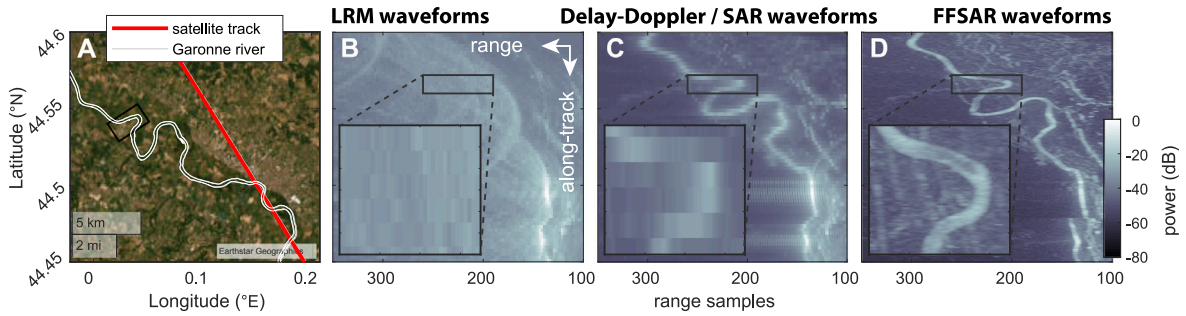

Fig. 1. The Garonne river as seen in different Sentinel-6 altimeter data products with varying along-track resolution due to differences in processing. Panel A shows the observation geometry. Panels B-D show the return signal in different altimeter data products: 20 Hz Low Resolution Mode (LRM) in which no SAR focusing has been performed (B), the 20 Hz SAR waveforms in which SAR focusing is performed over individual bursts of pulses (C) and the ~5917 Hz fully focused SAR waveforms, using a synthetic aperture of 2.2 s for SAR focusing (D). Single rows of the shown radargram are called waveforms.

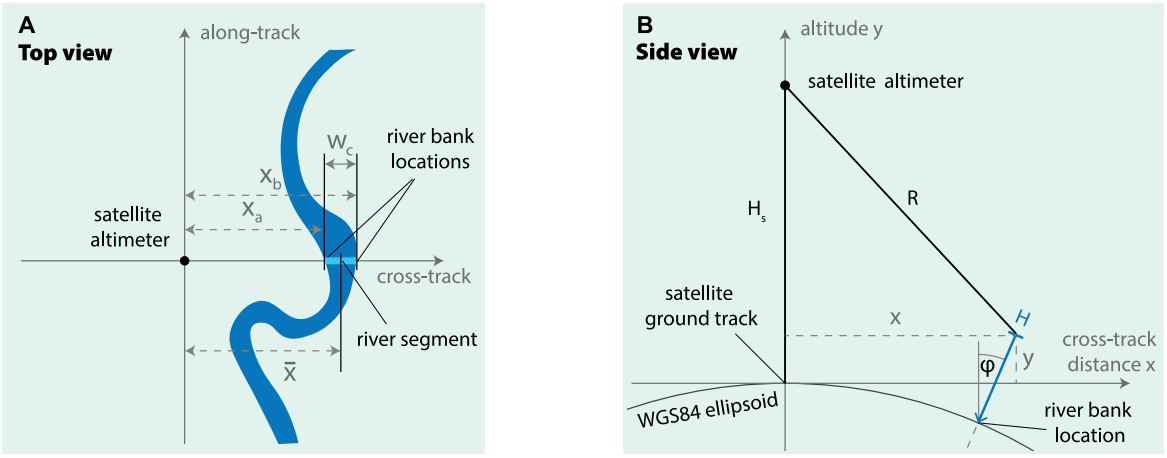

Fig. 2. Sketch of the observation geometry, including variable labels. The top view on the left-hand side shows a meandering river; the side view on the right-hand side shows the effects of Earth's curvature.

respectively. To illustrate the differences, we provide the LRM, SAR and FFSAR radargrams close to the Garonne river in France in Fig. 1. As expected, there is a bright signal peak in all radargrams when the river is located in (or close to) nadir (see satellite latitudes between 44.45–44.5 degrees North), from which the river water level H can ordinarily be calculated at the three river crossings according to the nadir altimetry equation

$$H = H_s - R, \tag{1}$$

with satellite altitude H_s and range R to the river's signal peak (assuming all instrument and geophysical corrections are applied to the range already). However, the SAR and FFSAR radargrams contain additionally a clean signal of the river segments at increased cross-track distances. Comparing the two products in the magnification panels (bottom half) we notice that only the FFSAR data can provide a high-contrast river echo in presence of meanders. Therefore, the FFSAR radargram potentially allows to compute slant ranges R to any river segment despite its cross-track distance, owing to the increased along-track resolution. This insight forms the bedrock of this work.

However, translating slant range into elevation is slightly more difficult in this slanted geometry, in which Eq. (1) is no longer valid. Therefore, the remainder of this section outlines how to calculate the water level of a single cross-track segment of the river, as shown in Fig. 2, top view. Instead of considering the extended segment right away, we consider an individual river bank in the side view of Fig. 2. The equations describing the geometry for a spherical Earth are

$$R^2 = (H_s - y)^2 + x^2, \tag{2}$$

$$y = (H + R_E)\cos\varphi - R_E, \tag{3}$$

$$x = (H + R_E)\sin\varphi, \tag{4}$$

with the slant range R, Earth's radius R_E and cross-track distance x to the river bank. Note that we treat the case of a spherical Earth to perform overseeable calculations. For all practical computations we use the ellipsoidal Earth; see Section 2.2 for details. One can try to solve this nonlinear system of equations directly for the desired river water level H. However, the proportions in Fig. 2 appear greatly distorted. Because H (~100 m) and x (~7 km) are small compared to the Earth's radius R_E (~6371 km) and satellite altitude H_s (~1340 km), the viewing angle towards any target in the footprint is actually no higher than 0.3°. This means that also φ is small, making H almost aligned with the y-axis and allowing for simplifications. As outlined in Appendix A, we can approximate H as

$$H = H_s - R + Kx^2, \tag{5}$$

with $K = (2H_s)^{-1} + (2R_E)^{-1}$. This result is a simple generalization of the nadir altimetry equation (Eq. (1)), but is generally valid for any cross-track target. Hence, we call it the off-nadir altimetry equation and refer to the term Kx^2 as the slant range correction. This generalized equation forms the centerpiece of the new measurement approach, as it allows to calculate water level all along the river instead of at the cross-overs only. This enables us in theory to obtain a dense river water level profile. All that is needed to calculate H from cross-track echoes is auxiliary knowledge of the river's cross-track distance x and — since K is small — we can often tolerate errors of several tens of meters in x without highly affecting the accuracy of the resulting river water level, which will be quantified in Section 2.3.3. Technically, we may also plug in an a-priori water level into Eq. (5) to estimate cross-track distance, but the sensitivity to errors is unfavorable in this scenario

($K^{-1/2}$ is large). Since we relied on approximations to obtain the off-nadir altimetry equation, it is worth mentioning that Eq. (5) has a systematic error of less than 1.2 mm for cross-track distances x smaller than 7 km using Sentinel-6 mission parameters, see Appendix A.

For now, we have considered one individual cross-section (associated to an individual waveform) that contains a single target at range R and cross-track distance x, as sketched in the side view of Fig. 2. However, rivers are extended targets, as shown in the top view of Fig. 2. Therefore, we propose extracting at least two ranges from one waveform with the following interpretation: The rise of the altimeter signal corresponds to the range towards the closest river bank R_a, whereas its decay provides the range to the farthest river bank R_b. In this notion, we can calculate the water levels at both river banks as

$$H_a = H_s - R_a + Kx_a^2 \tag{6}$$

$$H_b = H_s - R_b + Kx_b^2. \tag{7}$$

such that the water level of the river segment can eventually be defined as the average of both

$$\hat{H} = \frac{1}{2}\left(H_a + H_b\right). \tag{8}$$

Doing so has several benefits. On the one hand, the term Kx^2 is not linear in x. Therefore, evaluating the term separately at both river banks is more accurate than evaluating it e.g. at a river center $\bar{x} = (x_a + x_b)/2$, since $(Kx_a^2 + Kx_b^2)/2 \neq K\bar{x}^2$. Furthermore, the averaging helps to naturally suppress the retracker bias and the effects of slope between opposite river banks; see Sections 2.3.1 and 2.3.2 for details.

To summarize, we have outlined in this section how the river water level can be deduced from the slant ranges to the river banks in case they are located at arbitrary positions within the altimeter footprint. The calculations were sketched for a single waveform, but can principally be iterated along the ground track to yield densely-spaced measurements of river water levels. In the following section we describe our newly developed PICTA algorithm for river level profile retrieval, emphasizing on (i) how it achieves to measure full river water level profiles and (ii) how it successfully prevents issues arising from multi-peaked waveforms and clutter by using an auxiliary river polygon and the full radargram.

2.2. The PICTA algorithm for river water level profile retrieval

Throughout the previous section we implicitly assumed known which signal peak in the waveform (yielding R) belonged to the river segment of interest (providing x), while in reality this knowledge is lacking. This mapping becomes ambiguous as soon as there are multiple peaks or multiple river segments in a waveform, making several values for R and x possible. The presence of multiple peaks is an often-encountered trouble already in nadir SAR altimetry (Villadsen et al., 2016, and references therein) and usually leads to major height misestimations, also known as snagging. The situation becomes even worse in a PICTA framework, as the slant range correction can reach values up to $K \cdot (7000\ \mathrm{m})^2 \approx 22$ m. Therefore, associating a peak with the wrong target and cross-track distance can render the resulting river water level entirely meaningless. A major part of our PICTA algorithm is therefore tailored to unambiguously detect the river signal within the radargram in the first place, so to prevent these issues. The following paragraphs describe the retrieval algorithm in detail while Fig. 3 serves as a graphical guide. In the following paragraphs, we denote the waveform index (in along-track direction) as $i = 1, 2, 3, \ldots, N$ and the river bank index as $j = a, b$.

FFSAR processing – To generate FFSAR waveforms, we rely on the back-projection algorithm implementation developed for CryoSAT-2 by Kleinherenbrink et al. (2020a) and refined for Sentinel-3 and Sentinel-6 by Ehlers et al. (2022). The FFSAR waveforms were generated using a synthetic aperture of 2.2 s. With Sentinel-6, this corresponds to an along-track resolution of 97 cm on the ground at the considered latitudes, which is equivalent to the posting rate (ground spacing in the data). However, we applied a Hamming window in both, range (over the whole receiving window) and azimuth (over the whole aperture) to suppress side lobes of the focused radar point target response, slightly reducing the effective azimuth and range resolutions. Prior to range compression, the waveforms were zero-padded to yield 512 instead of 256 range samples, in line with the official L1b high-resolution product disseminated by EUMETSAT, so that the range gate spacing becomes $\delta r \approx 18.97$ cm (EUMETSAT, 2021).

Reading polygon and altimeter data – The auxiliary river polygon and the FFSAR radargram recorded during a single satellite overpass are read (see panels A and B in Fig. 3). Both the polygon and the satellite data are provided over the WGS84 reference ellipsoid. We apply a ten-waveform moving-average filter, corresponding to ~10 m along track to reduce the speckle noise level in the FFSAR radargram. Hence, the along-track resolution of the final river water level product is also about 10 m. We keep the posting rate of 1 m, however, because it is known that the noise in the output of a threshold retracker may decorrelate faster than the SAR along-track resolution (Ehlers et al., 2023).

Finding polygon intersections – We need to find the cross-track distances $x_{i,j}$ between the satellite position and the river segments along the entire ground track. At each along-track satellite location i, we first project the river polygon into the local Cartesian East-North-Up coordinate system, assuming zero elevation $H = 0$. Then, we approximate the FFSAR footprint as a line oriented in cross-track direction, centered around the origin (the nadir point). Thereafter, we find the intersection of the footprint and the river polygon within the East-North plane, which provides the East and North coordinates of all intersected river banks. Note that multiple intersections may exist in the presence of meanders (see Fig. 3). The cross-track distances $x_{i,j}$ are computed from the distances between these points and the origin. For all intersected river banks, we need to perform the transform of the points $(E, N, U = 0)$ back into ellipsoidal coordinates to obtain the altitude offset at the off-nadir positions due to the ellipsoid's curvature. This offset replaces the term $x^2(2R_E)^{-1}$ for a spherical Earth in Eq. (5).

Initial guess of river signal – Having obtained $x_{i,j}$, we can use Eq. (5) to calculate the range samples $r_{i,j}$ at which to expect the river banks from

$$R_{i,j} = H_{s,i} - H_{\mathrm{init}} + Kx_{i,j}^2 = \delta r(r_{i,j} - r_{\mathrm{ref}}) + R_{\mathrm{trk},i} \tag{9}$$

given the reference range gate $r_{\mathrm{ref}} = 257$ (1-based indexing), the tracker range setting of the altimeter R_{trk} and a constant initial guess of the river water level H_{init}, see Fig. 3B. As Eq. (9) explicitly includes the tracker range, waveform alignment is not necessary prior to PICTA processing. As the water level of a river typically varies much less than the width of the altimeter's receiving window (~100 m), the initial guess H_{init} can be chosen once manually per river case, e.g. via a digital elevation model. Although the shown initial guess is not matching the signal yet, the figure illustrates well how the auxiliary river polygon predicts the target's two-dimensional signal shape—its"fingerprint"—within the radargram, as meanders and curves are already well reproduced, compare black line and bright signal in Fig. 3B.

River signal detection – To further align the signal and the initial guess from the river polygon, we assume H_{init} to consist of an offset H_0 and slopes $\mathrm{d}H_N = \mathrm{d}H/\mathrm{d}lat$ and $\mathrm{d}H_E = \mathrm{d}H/\mathrm{d}lon$ with latitude and longitude of the river banks, respectively, to approximately describe the river's elevation and inclination as

$$H_{\mathrm{init},i,j} = H_0 + \mathrm{d}H_N \cdot lat_{i,j} + \mathrm{d}H_E \cdot lon_{i,j}. \tag{10}$$

A justification for this simple linear model is provided at the end of the paragraph. It must also be stressed that this model will not be explicitly used within the retracking in a later step. As before, we can find the range samples $r_{i,j}$ at which to find the river banks as a function of H_{init} from Eq. (9), which provides one minimum and maximum range for each river intersection in each waveform, $r_{i,a}$ and $r_{i,b}$, respectively.

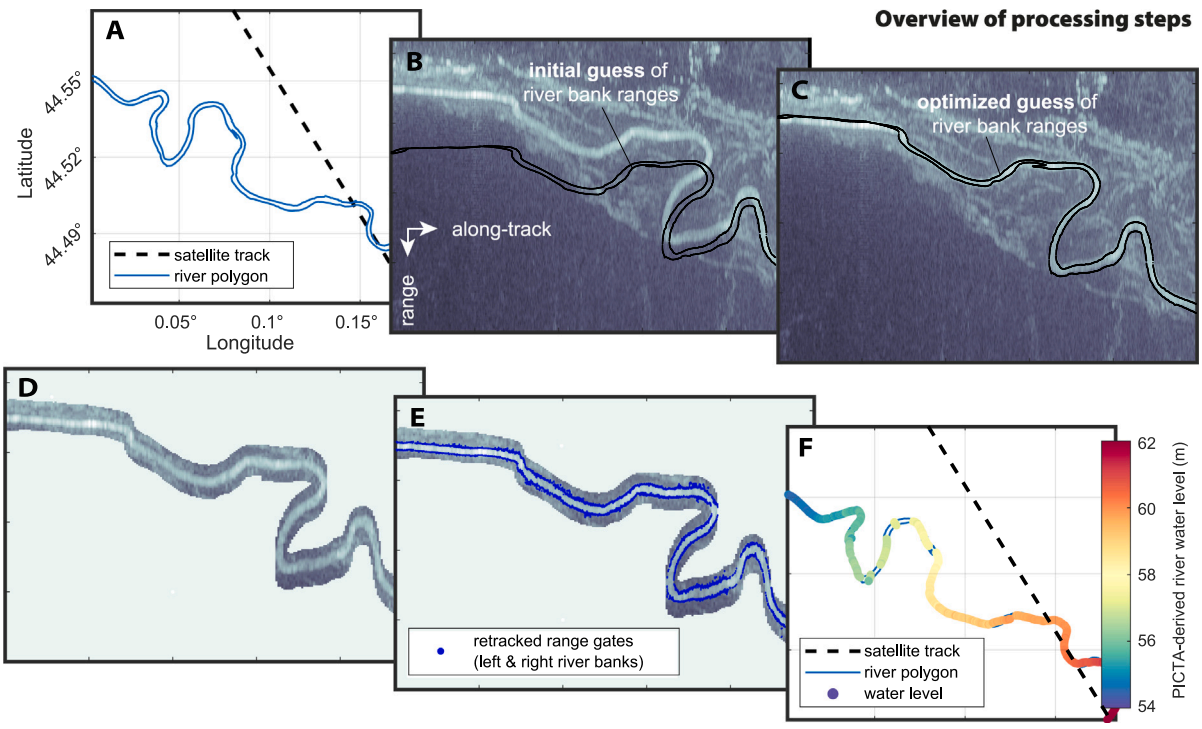

Fig. 3. Illustration of the PICTA processing steps needed to obtain a river's water level profile (panel F) over the WGS84 reference ellipsoid. The PICTA algorithm starts from an a-priori river polygon (panel A) and the FFSAR-processed altimeter signal (panel B). The steps are described in Section 2.2.

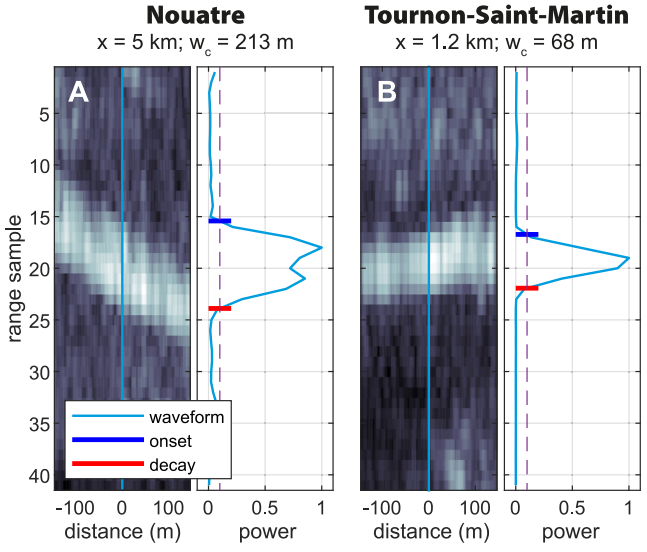

Fig. 4. FFSAR waveforms around two different river-gauge locations (see Fig. 6), both shown as heat maps (left) and line plots (right). The river's signal at Nouatre is widened compared to Tournon-Saint-Martin, due to the combined effect of an increased cross-track river width $w_c = x_b - x_a$ at an increased cross-track distance. The dashed line marks the applied threshold of 0.1. Note that the width of the signal in units of range samples $w_r = r_b - r_a$ can be estimated via Eq. (9) to be $w_r = K(x_b^2 - x_a^2)/\delta r = 2K(x_b - x_a)(x_b + x_a)/(2\delta r) = 2Kw_c\bar{x}/\delta r$, which yields $w_r = 5.04$ for Nouatre and $w_r = 0.39$ for Tournon-Saint-Martin. These estimates are consistent with the plots, considering the width of the instrument's range point target response itself is 4.84 range gates at 0.1 threshold.

The log-power of the radargram (waveforms) $\log_{10} P_{i,r}$ (with waveform index i and range sample r) should be high in between those range samples. The same holds true for the power itself, but the log-power is a more robust measure since the river signal magnitude may vary significantly with cross-track distance and local surface conditions, i.e. due to the paired influences of the antenna gain pattern and the local mean square slope of the water surface (see e.g. Boy et al., 2022). So to automatically locate the river signal in the radargram $P(i, r)$, we maximize the objective

$$\max_{H_0, \mathrm{d}H_N, \mathrm{d}H_E} \sum_i \sum_{r_{i,a}-r_{\mathrm{buffer}}}^{r_{i,b}+r_{\mathrm{buffer}}} \log_{10} P(i, r), \tag{11}$$

with respect to offset and slopes and using a Nelder–Mead simplex algorithm (Lagarias et al., 1998). If we summed the log-power only in between $r_{i,a}$ and $r_{i,b}$, the optimizer may be unable to reliably detect the signal in presence of variable river slopes and discontinuities such as dams, because the simple linear model of H_{init} in Eq. (10) is too restrictive. On the other hand, the optimization parameter space should not become too large, either, not to deteriorate performance. To circumvent both problems, we allow for a buffer range $r_{\mathrm{buffer}} = 7.5$ range gates in the summation of the objective function (11), so that the signal detection algorithm may robustly handle discontinuities up to 15 range gate samples, equivalent to level differences of at least 2.85 m. The resulting fit is shown in Fig. 3C.

Signal cropping – We crop the waveforms to the parts that contain the river signal for further processing, see Fig. 3D. In doing so, the retracker is much less likely to get trapped by another bright signal within the scene that is not the river (clutter, secondary water bodies). For the cropped waveforms (called subwaveforms in the following), we allow for a buffer of 10 range samples, see Fig. 3D. We may identify multiple subwaveforms per waveform (one column of the two-dimensional signal) as illustrated in the right-hand side of this figure.

Threshold retracking – In the following, the subwaveforms are retracked using a tailored variant of a threshold retracker (Laxon, 1994) with a threshold value of 0.1. First the subwaveform is normalized by the maximum. Subsequently, all waveform segments above the threshold value are identified. We first disregard all candidate segments directly at the boundaries of the subwaveform and finally choose the candidate segment with the highest power per range sample from the remainder. We then determine the retracked ranges of the two river

banks from the two floating-point range samples at which the linearly interpolated waveform segment exceeds the threshold and falls below it, respectively, see blue and red marks in Fig. 4. The results of this step are illustrated in Fig. 3E.

Note that our choice of the threshold value is not arbitrary but motivated by the expected speckle noise level after averaging of 10 along-track resolution cells, see Appendix B.

Applying geophysical corrections – All the resulting ranges are adjusted using the geophysical corrections contained in the Level-2 data files from EUMETSAT. We apply the modeled dry and wet tropospheric corrections at measurement altitude, the ionospheric correction, the solid Earth tide correction, the pole tide correction, and the modeled instrumental range correction. Since the corrections are provided at either 1 Hz or 20 Hz posting rates along the satellite's ground track, we interpolate them linearly to match the FFSAR posting rate of ~5917 Hz. Thereafter, all water levels are adjusted using the geophysical correction values along the ground track and regardless of the river's cross-track distance.

River water level estimation – The resulting ranges are transformed into river water level using Eq. (5) but replacing the term $x^2(2R_E)^{-1}$ as described in step **Finding polygon intersections**. Subsequently, the water levels of opposite banks are averaged according to Eq. (8) to yield a reliable estimate. The resulting river water level profile is plotted in Fig. 3F.

Quality flagging – Finally, two quality flags are checked to disregard erroneous measurements. First, close to the nadir or within the turns of a meander, we may identify multiple but overlapping subwaveforms. In those cases, there may be two or more river echoes within one subwaveform, so the retracking results are ambiguous (as either of both peaks may be chosen), and so is the correct choice of x for the slant range correction. Therefore, the river water level is generally considered invalid in such situations. Furthermore, the optimized first guess (Fig. 3C) provides us with an estimate of the expected river signal width Δr^* (in terms of range samples). If we add a buffer of 3 samples to account for the blurring due to the point target response in range, then we can compare Δr^* to the retracking results $\Delta r_{\text{retracked}} = (R_b - R_a)/\delta r$. Followingly, we flag all river water levels invalid if the difference between both becomes too large, namely if

$$|\Delta r_{\text{retracked}} - (\Delta r^* + 3)| > 4, \tag{12}$$

so that mistakenly too-narrow river signals (e.g. due to a pronounced speckle noise peak) or too-wide river signals (e.g. due to additional clutter in the leading or trailing edges) are not considered valid. This criterion will also flag the estimates invalid whenever the river considerably overflows its banks in a high-water situation. It must be stressed that the value of four has been defined heuristically and may need adjustment in case of another windowing strategy within the SAR focusing, in case of altered zero-padding in range or considering other altimeter mission parameters.

Additional comments – We mentioned beforehand that the algorithm is semi-automated, because there are two steps that need special attention. Firstly, the auxiliary river polygon data was manually downloaded and reviewed for both case studies, see Section 3. Secondly, the optimization results in **River signal detection** is typically dependent on the initial parameter values of H_0, $\mathrm{d}H_N$ and $\mathrm{d}H_E$; it was possible in both case studies to choose initial values that led to poor performance, particularly when the initial guess covered another water target such as the Canal latéral à la Garonne, causing the optimizer to be trapped in a local maximum.

2.3. Additional error sources in PICTA

The error budget of the new measurement approach differs from the nadir measurements in some aspects, most noticeably because the measurement of river water level via the off-nadir altimetry Eq. (5) requires knowledge of the river's cross-track distance. Two more indirect aspects that should not go unmentioned here are those of retracker bias and river slope. We will quantify the sensitivity of the river water level for each aspect in the following subsections, which may be as small as a few millimeters to a few centimeters for most parts of the 14 km swath unless the river becomes too wide or the river polygon becomes too inaccurate.

2.3.1. Retracker biases

The range estimation from the waveforms can be performed in many different ways and we may generally obtain range biases depending on the applied retracking strategy (see e.g. Dinardo, 2020; Kleinherenbrink et al., 2020a; Villadsen et al., 2016), even if a numerical retracker was used Boy et al. (2022). In this work, we applied a tailored threshold retracking (Laxon, 1994); see Section 2.2. The choice of the retracker's threshold may bias the measured range to the river banks by several decimeters; compare to Fig. 4. We denote the retracker bias ΔR so that the measured range is written $R = R^* + \Delta R$ with the true range R^*. Replacing R in Eqs. (5) and (8) yields

$$\hat{H} = \frac{1}{2}\left(H_a + H_b - \Delta R_a - \Delta R_b\right) \tag{13}$$

with ΔR_a and ΔR_b the retracker biases at the respective banks. At first glance the retracker bias seems to directly contribute to water level bias — but ΔR_a and ΔR_b have opposite signs by design of the retracking procedure, since we infer the distance to the nearest river bank a from the rise of the altimeter signal and the distance to the farther river bank b from its decay. This is best verified from Fig. 4: Lowering the threshold takes the opposite effect on either bank, as the nearest one will appear closer and the farther one further away from the altimeter. So unless the average shape of the waveform's trailing edge (signal decay) and leading edge (signal rise) differs systematically, we can write $\Delta R_b = -\Delta R_a = \Delta R$ so that the estimated river water level $\hat{H}$ is indeed free of any retracker bias. We must stress that this assumption may be violated for wide river segments, since the leading and trailing edge will be modulated differently along x, e.g. by the altimeter's antenna gain pattern. Note also that the retracker bias may generally vary along the river, as the river's signal shape is changing with, e.g., the river width, river curvature, the river's cross-track distance and the river's orientation relative to the satellite ground track.

2.3.2. Cross-track river slope

One added benefit of measuring a river water level profile is the information of river slope. At the same time, ignoring the inclination of the river within the data processing may seriously decrease the accuracy of the water level estimates (for a related example see Halicki et al., 2023). Therefore, we must stay aware that H_a and H_b in Eq. (8) may differ. Due to the limited width of rivers, we assume in the following that the difference between H_a and H_b can be well described by a constant cross-track river slope $m_x = \frac{\mathrm{d}H}{\mathrm{d}x}$. H_a and H_b can then be written as

$$H_a = H_{\text{center}} - m_x \frac{x_b - x_a}{2} \tag{14}$$

$$H_b = H_{\text{center}} + m_x \frac{x_b - x_a}{2} \tag{15}$$

with H_{center} the river elevation at the center of the segment $\bar{x} = (x_a + x_b)/2$. Similar to the retracker bias, also the terms containing the cross-track river slope m_x cancel out in Eq. (8), and we obtain

$$\hat{H} = H_{\text{center}}, \tag{16}$$

meaning that the estimated river water level represents the elevation at the center location $\bar{x}$ of the river segment. Although the difference between H_a and H_b could technically be used to infer the cross-track river slope from the FFSAR data, this would require the knowledge of the retracker bias in the first place.

2.3.3. Uncertainties in cross-track distance

A rigorous implementation of PICTA required for each overpass the corresponding river polygon — which is generally not available. There is the possibility to derive water masks from imagery, but only at limited resolutions, with limited geolocation accuracy and accepting an offset in time due to different revisit periods. Therefore, this section discusses the sensitivity of the estimated river water levels to errors in the cross-track distance, which originate from the uncertainty of the river polygon information.

Similar as for the range beforehand, we write the difference between the assumed river bank cross-track distances x and the respective truth x^* as Δx and write $x = x^* + \Delta x$. Following Eqs. (5) and (8), we can attribute an error in river water level $\Delta H = \hat{H} - H_r^*$ to this difference, which reads

$$\Delta H = \frac{K}{2}\left(2x_a^*\Delta x_a + 2x_b^*\Delta x_b + \Delta x_a^2 + \Delta x_b^2\right). \tag{17}$$

It will be useful in the following sections to express ΔH in terms of river midpoint $\bar{x} = (x_b^* + x_a^*)/2$ and the true cross-sectional river width $x_b^* - x_a^* = w_c^*$ (the width of the river segment along the cross-track direction)

$$\Delta H = \frac{K}{2}\left(2(\bar{x} - w_c^*/2)\Delta x_a + 2(\bar{x} + w_c^*/2)\Delta x_b + \Delta x_a^2 + \Delta x_b^2\right), \tag{18}$$

compare to Fig. 2 for clarity.

Modeling both Δx_a and Δx_b in Eq. (18) as independent normal random variables with zero mean $\mathbb{E}[\Delta x] = 0$, and standard deviation $\sigma_x = \sqrt{\mathbb{E}[\Delta x^2]}$ yields a small bias of

$$\mathbb{E}[\Delta H] = K\sigma_x^2, \tag{19}$$

which is 4.5 mm for a relatively high error of $\sigma_x = 100$ m, and only 0.045 mm for $\sigma_x = 10$ m. The standard deviation of ΔH is given by

$$\sigma_{\Delta H} = K\sigma_x\sqrt{2\bar{x}^2 + \frac{w_c^{*2}}{2}}, \tag{20}$$

which is dependent on river width and cross-track distance of the river midpoint, though dominated by the latter in most cases. Fig. 5 shows the uncertainty $\sigma_{\Delta H}$ depending on w_c^* and x, assuming a value of $\sigma_x = 10$ m, which are below 5 cm. If we assumed $\sigma_x = 20$ m instead, the uncertainty would be less than a decimeter (remember the linear dependency in Eq. (20)).

The dependence on the cross-sectional river width w_c^* also implies that the river water level estimate becomes inaccurate for rivers oriented almost orthogonal to the ground track: For a straight river segment with width w^*, directed at an angle α with respect to the satellite's ground track we get

$$w_c^* = \frac{w^*}{|\cos\alpha|}, \tag{21}$$

which can be plugged into the previous Eq. (20) to estimate uncertainties and systematic errors depending on α. Since w_c^* diverges towards $\alpha = \pi/2$, so does the error in H. Therefore, the accuracy of the obtained water level is generally highest for river segments that are directed parallel to the ground track and worsens with increasing inclination α.

In summary, already moderately accurate mapping data with errors between 10–20 m can provide river water levels with less than 1–10 cm additional error compared to nadir measurements.

3. Data

3.1. Case studies

Two case studies are selected to demonstrate our PICTA algorithm, shown in Fig. 6. The selection criteria for the choice of the study areas were:

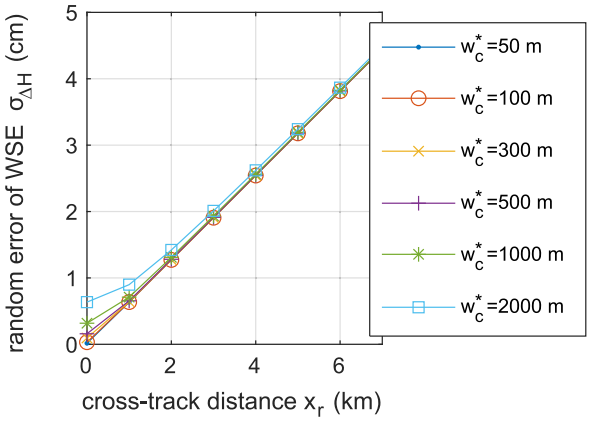

Fig. 5. Random error in river water level H in dependence of cross-track distance to the river's center and cross-sectional river width, according to Eq. (20) and Sentinel-6 mission parameters. The graph assumes an uncertainty $\sigma_x = 10$ m for the cross-track distances.

1. Preferably long river stretches within the satellite footprint (>30 km).
2. Availability of multiple referenced river gauges for validation of the river water level profiles.
3. A good representation of different parameter values for cross-track distances x (the whole swath of 0–7 km) and cross-sectional river widths w_c (30–300 m) at the in-situ stations, as these were identified previously to impact the accuracy and precision.
4. Availability of additional validation data.
5. Absence of expanded secondary water targets such as wetlands and extensive irrigation infrastructure, meaning e.g. densely packed ditches, in order to ensure contrast (see Section 5).

We chose both cases in France since the rivers are densely monitored by gauges with reliable height references. The first case is a Sentinel-6 overpass from North-West to South-East above the Garonne river (see panel A of Fig. 6). The track segment shown is longer than 35 km, and three river gauges are located within the swath. The second case is a Sentinel-6 overpass from North-West to South-East, flying mainly over the Creuse river, but also capturing parts of the Venant, Gartempe and Anglin rivers (see panel B of Fig. 6). The Creuse river and its tributaries are oriented neatly along the satellite's track over a distance greater than 60 km, such that nine validation sites fall within the satellite swath, which allows to evaluate the PICTA algorithm performance in the presence of multiple river segments. The averaged cross-track distances x and the cross-sectional river widths w_c at all in-situ stations are collected in Table 1, providing a balanced representation of cross-sectional widths between 44–266 m and cross-track distances between 0.4–7.6 km.

To assess the accuracy and precision of the altimeter-derived river water level profiles, we process the Sentinel-6 altimeter data over the study areas within the full two-year period of 2021–2022. Considering the satellite return period of 10 days, this provides 73 overpasses. However, we found that some files in early 2021 do not contain the relevant pulse data at the locations of the overpasses. We speculate that this may be due to orbit maneuvers or problems with the data downlink. However, a total number of 56 and 57 useful overpasses remain over the Garonne and Creuse rivers, respectively.

3.2. Sentinel-6 altimetry data

We obtained the raw IQ samples (complex-valued pulse data, within Level-1a product) of the Sentinel-6 radar altimeter from the EUMETSAT Datastore https://data.eumetsat.int. We used the most recently

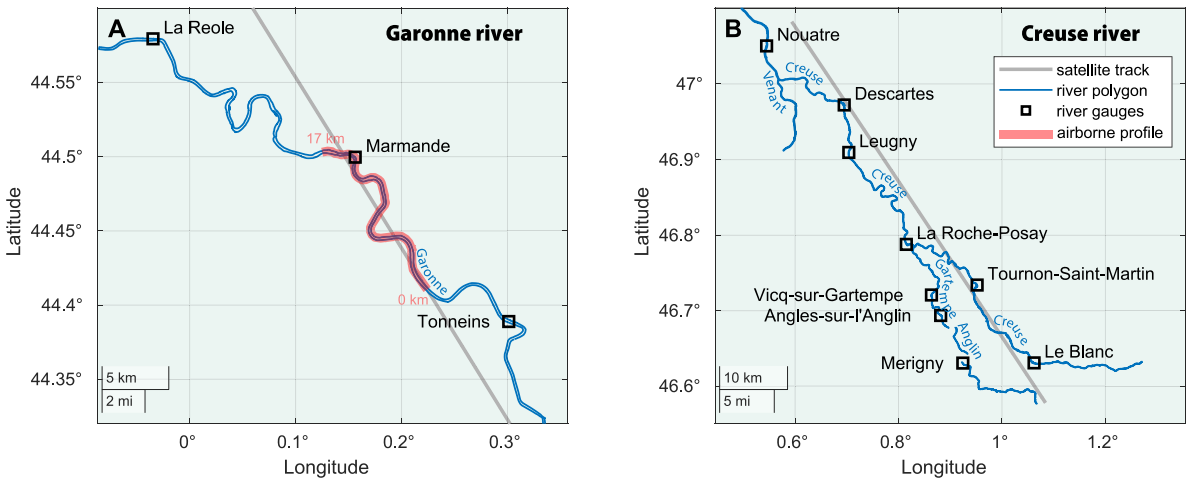

Fig. 6. Maps of the two study areas. The left panel shows a segment of the Garonne river in France, and the right panel shows mainly the Creuse river, including most of its bifurcations. The rivers are shown with blue lines, squares indicate the location of river gauges with available reference measurements, and the satellite ground track is shown as a gray line. The red line marks the segment of the river over which an airborne measurement of vorteX.io is available. (For interpretation of the references to color in this figure legend, the reader is referred to the web version of this article.)

Table 1
Statistics of the comparison between PICTA-derived and in-situ river water levels at the river gauge locations. Note that the mean bias and standard deviation (STD) were calculated omitting the outliers. The median bias and the scaled median absolute deviation (MAD) were calculated including the outliers.

Site	Parameters:		Biases (cm):		Errors (cm):		Number of observations:		
	x (km)	w_c (m)	Mean	Median	STD	Scaled MAD	Valid	Invalid	Outliers
Le Blanc	1.8	110	3.6	2.7	3.6	4.2	56	1	9
Tournon-Saint-Martin	1.2	68	1.7	1.8	2.6	2.6	57	0	0
La Roche-Posay	4.1	87	1.4	1.3	3.8	3.8	57	0	0
Leugny	3.7	107	10.2	9.4	6.7	6.7	56	1	1
Descartes	0.4	141	19.1	18.8	3.6	4.1	57	0	1
Merigny	7.0	44	−2.8	−2.0	7.2	6.6	51	6	2
Angles-sur-l'Anglin	5.7	60	−1.9	−2.0	6.3	5.9	54	3	1
Vicq-sur-Gartempe	5.2	126	2.1	0.8	6.3	6.9	57	0	0
Marmande	0.5	154	2.9	2.6	5.2	4.6	55	2	1
La Reole	7.7	266	0.4	6.7	12.0	10.0	7	50	0
Tonneins	3.9	252	−0.5	−0.7	5.2	5.4	57	0	0
Nouatre	5.0	213	4.0	3.4	6.1	4.4	43	14	3

reprocessed data product, i.e. from the collection "Poseidon-4 Altimetry Level 1 A High Resolution (baseline version F08) - Sentinel-6 - Reprocessed" with collection ID EO:EUM:DAT:0838. The geophysical corrections, such as wet tropospheric delay and the ionospheric correction, are obtained from the associated Level-2 product "Poseidon-4 Altimetry Level 2 High Resolution (baseline version F08) - Sentinel-6 - Reprocessed" with collection ID EO:EUM:DAT:0841.

3.3. Auxiliary data

River Polygon Data – All river polygon data used within this research, see, e.g., Figs. 1, 6, 7 and 11, have been exclusively obtained from OpenStreetMaps. We refer the reader to for the data sources and details of the ODb License.

River Gauge Data – The river gauge data used for this research has been obtained from the HydroPortail Service of Eaufrance (https://www.hydro.eaufrance.fr/), which collects and disseminates hydrological data for the entire France. All stations' coordinates and reference levels have been transformed from Lambert 93 (EPSG:2154) to WGS84 (EPSG:4326) and from NGF-IGN69 (EPSG:5720) to WGS84, respectively, prior to usage. Of all available water level data at a station (raw, pre-validated, validated), the most validated have been chosen.

vorteX.io Data – vorteX.io (https://www.vortex-io.fr/en/) provides a real-time hydrology measurement service based on a new generation of innovative and intelligent remote sensing solutions. In the climate change context and the associated increasing number of natural risks and, more specifically, flooding events, vorteX.io has designed a lightweight remote sensing instrument (Lidar), inherited from the specifications of radar altimeters on board altimetric satellites, capable of providing water height measurements with centimeter-level accuracy and at high frequency, see Fouqueau et al. (2022) for more details on the airborne system. VorteX.io offers a range of services based on this innovative, connected, autonomous, and cost-effective instrument that can be integrated into a flying drone or considered a fixed in-situ station for monitoring hydrological systems. VorteX.io systems are the results of a review of existing in-situ systems used for Cal/Val of satellite altimetry in hydrology. As vorteX.io remote sensing instruments are inspired by satellite altimetry, water level measurements are directly comparable to satellite altimeter data.

4. Results

In the following two sections, we will evaluate the biases and uncertainties of the PICTA river levels compared to the river gauge readings. We will evaluate parts of the Garonne River profile against the vorteX.io airborne lidar data.

4.1. Validation against river gauges

A single measurement of both river water level profiles is provided in Fig. 7, left-hand side. All profiles show only a few small data gaps and the color gradient across the profile shows the river slope. On

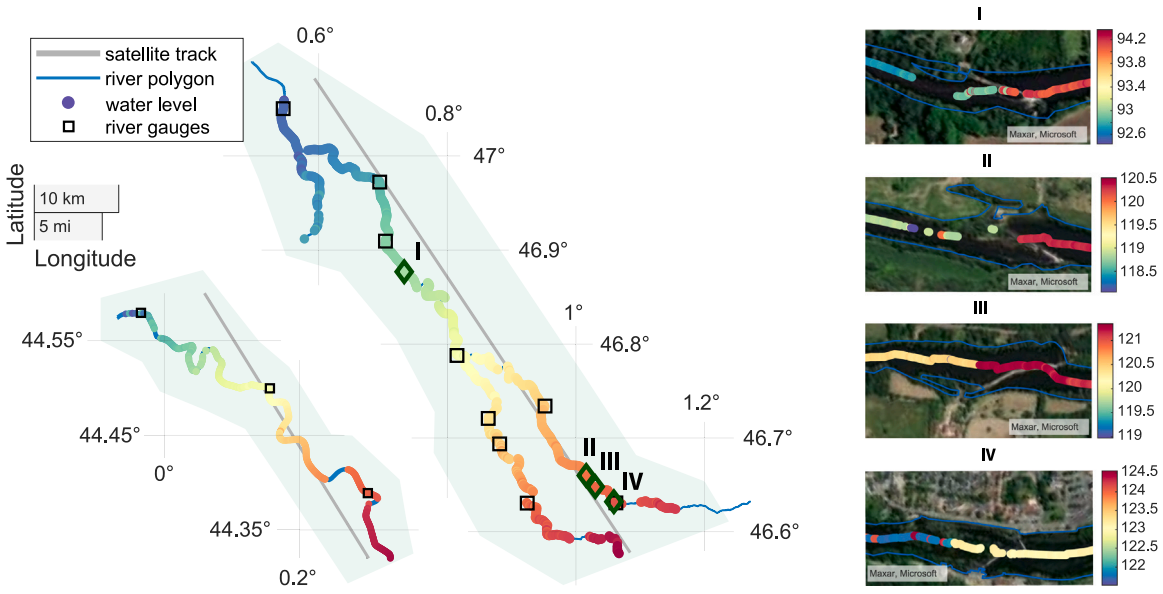

Fig. 7. PICTA-derived river water level profiles over the WGS84 reference ellipsoid for the two case studies in Fig. 6. For each overpass, the algorithm produces an entire map of river water level over the input river polygon; see left-hand side, as long as the river is within the swath. The river gauges are illustrated by black squares, as in Fig. 6. Four zoomed panels on the right-hand side show the quality-flagged data at 10 m resolution near dams (diamonds in the map), capturing the abrupt changes in river water level. Note that some outliers remain on the 10 m resolution product since no median filter was applied. Also, the estimates may be flagged invalid when multiple channels are too close to each other and cannot be distinguished, hence the data gaps in cases I and II. (For interpretation of the references to color in this figure legend, the reader is referred to the web version of this article.)

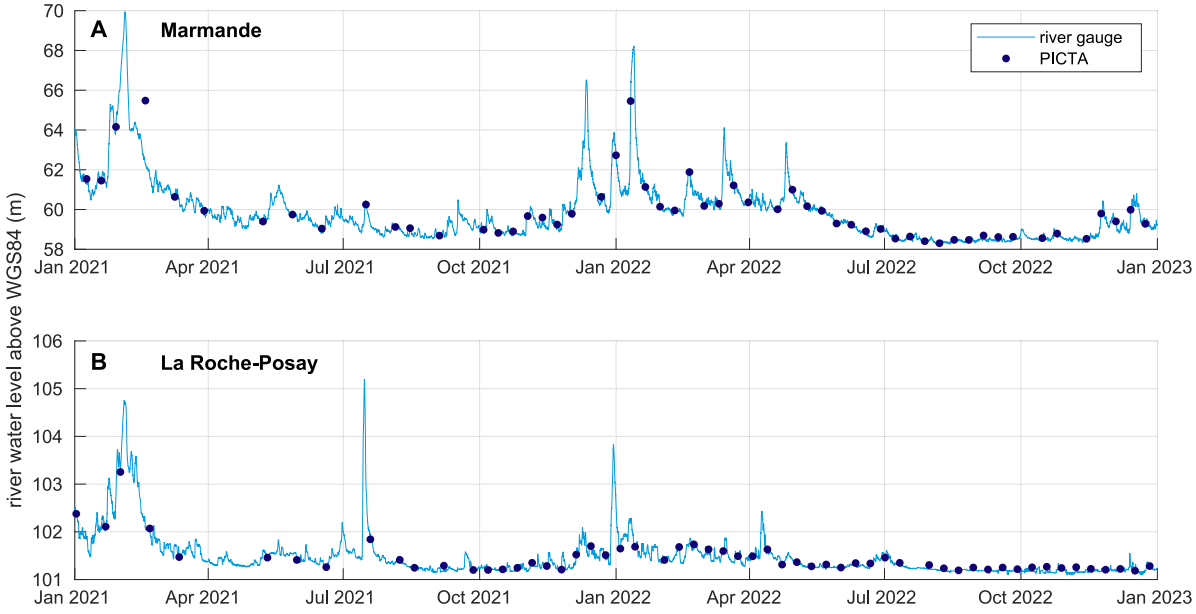

Fig. 8. River water level time series over a single river gauge from each of the case studies, see Fig. 6. The altimeter-derived water level is plotted with dark blue dots. The prominent data gaps within the first year are not caused by outlier filtering but by an absence of radar pulse data.

a local machine, PICTA processing of a single Garonne profile took approximately 8 s on 10 m and 60 s on 1 m along-track spacing. For the Creuse, a single profile took approximately 60 s on 10 m and 215 s on 1 m along-track spacing to generate. In the current implementation, the highest computational cost is caused by the step **Finding polygon intersections**, in which the whole river polygon is reprojected and intersected several ten thousand times (at each along-track location). Using an appropriate projected coordinate reference system in which to process the entire scene, and partitioning the polygon beforehand, will likely improve the performance.

For a comparison with the river gauges, we filter the altimeter data using a median over all altimeter samples within a 10 m radius around the altimeter sample closest to the river gauge. This is deemed necessary, since the altimeter data will inevitably show at least some outliers due to clutter or pronounced speckle peaks. Taking into account the 10 m moving average and the radius of the median-filter, the PICTA-derived river water level used for comparison contains information of at most 30 m along the track.

Fig. 8 shows the gauged and PICTA-derived water levels at one river gauge location in each study area. In both cases, the winter periods are characterized by increased water levels, presumably due to increased precipitation. On the other hand, water levels are at their minimum during the end of summer and autumn of 2022. The water level shows

temporal variability on time scales shorter than 10 days; hence, the Sentinel-6 altimeter alone does not capture all peaks or troughs.

Using similar time series at all river gauges, we compiled the statistics presented in Table 1, showing both mean and median statistics for bias and random errors. Here, STD denotes the standard deviation of the errors and the scaled MAD denotes their scaled Median Absolute Deviation

$$\text{scaled MAD}[X] = 1.4826 \cdot \text{M}\left[|X - \text{M}[X]|\right] \quad (22)$$

with median $M[...]$. Note that the scaled MAD itself is a consistent estimator of STD when the error obeys a Gaussian distribution, while being much less affected by few outliers than the STD in practice. Therefore, we removed a small number of outliers only for the computation of the mean statistics, i.e., mean bias and STD (see column outliers), while the outliers remained for the computation of the median statistics, i.e., median bias and scaled MAD. We consider a PICTA-derived river water level value H an outlier if it lies beyond $4 \cdot$ MAD of the time series $H - H_{gauge}$. Talking for all stations but Descartes, Leugny and La Reole for the moment, the mean and median biases are on the order of only 0–4 cm, while STD and MAD are between 3–8 cm. As shown in Fig. 5, an error in the river polygon on the order of 10 m may cause an error in water level between 0–4 cm, depending on cross-track distance. We considered inaccuracies of the river polygon as random errors in Fig. 5 with respect to the whole river profile. Yet, when repeatedly sampling the same location over time, we repeat the same error from the a-priori river polygon so that any inaccuracy will locally manifest as a bias. Therefore, the obtained biases between −4 to 4 cm agree with the expected error budget from Fig. 5. We discuss the remaining stations in the following.

The station of La Reole could only be sampled when the instrument was not operating in RMC mode (for clarification see EUMETSAT, 2021) because it was otherwise located too far cross-track. Therefore, only seven valid points are available, which is too few to compute reliable statistics, and thus, noticeable discrepancies arise between mean and median estimates of bias and uncertainty.

The PICTA-derived river water level performs well at Leugny and Descartes regarding random errors but shows mean biases of about 10 cm and 19 cm, respectively. Upon checking the nearby river polygon at Leugny against satellite imagery, it appears that the shadow of the bridge where the gauge is located has been erroneously interpreted as a river bulge. This is likely contributing to the bias at Leugny station. We likewise inspected the river polygon at Descartes but could not identify an obvious cause for the high bias.

4.2. Validation against airborne lidar

For the Garonne River we were provided by CNES with a river water level profile measured by an airborne lidar of vorteX.io, called lidar-derived profile for brevity hereafter. The flight trajectory is shown as red line in Fig. 6. This lidar-derived profile was measured over the course of 3 h, while the corresponding satellite overpass took only a few seconds. Therefore, the profiles are not precisely co-located in time. Since the in-situ river gauge readings show variations on the order of centimeters within this 3 h time frame, we do not consider the lidar-derived profile measurement for bias determination. In spite of that, we obtain a STD of 6.2 cm and a scaled MAD of 5.0 cm between the PICTA-derived and the lidar-derived profiles of river water level, indicating a good agreement. Because the PICTA-derived measurements are located along the river's center with respect to the cross-track direction, they cannot be perfectly co-located with the piece-wise straight trajectory of the airborne lidar. Followingly, we needed to choose a rather large co-location radius of 100 m around the lidar trajectory, as the river widths varied between 200–300 m. As before, the PICTA-derived river water level is computed from a median (of up to maximally 200 samples) around each point along the lidar's trajectory. Lidar points with less than 50 valid PICTA samples in their vicinity have been omitted from

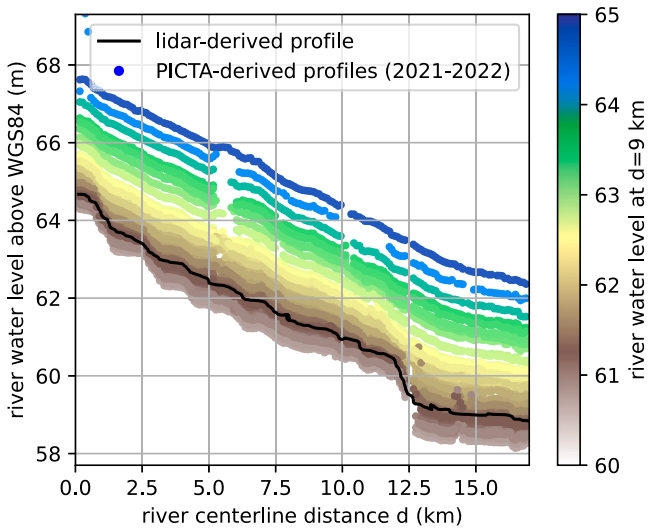

Fig. 9. PICTA-derived river water level profiles recorded during 2021–2022 along the marked segment of the Garonne river, see red line in Fig. 6. The profiles are colored according to their offset at centerline distance d = 9 km. The lidar-derived profile (black line) shows the same local slopes, which are varying with water level.

the analysis. The lidar-derived river water level profile is shown as black line in Fig. 9 along with the PICTA-derived profiles from the 2 year period, colored according to their height offset. The data indicates that the local river slope changes with water level: At low water levels (brown), the river water level exhibits small-scale irregularities seen in both the PICTA-derived and the lidar-derived profiles as it creeps over its bed, while at high water level (blue) the profiles are much smoother. The most prominent feature is a steep descent located around 12.5 km. As the water level increases, the river bed itself becomes less dominant in the water surface slope and the surface varies more smoothly with centerline distance.

The ability to obtain this type of measurements from a nadir radar altimeter is a unique feature of the PICTA approach and marks a milestone in nadir altimetry data processing. Previously, river slopes could only be assessed implicitly, see e.g. Calmant et al. (2013), Birkinshaw et al. (2014) and Schwatke et al. (2023), either by assuming a constant slope between virtual stations or by applying more elaborate (statistical) interpolation schemes, or Halicki et al. (2023) who approximated a temporally constant slope at each VS by using the orbital variation of the satellite platform. Any discontinuity or obstacle in the river such as natural water falls, rapids or artificial dams, makes an assessment using the first-mentioned approach very difficult, if not impossible. It is worth mentioning the ICESat −2 mission at this point, although it deploys a lidar, since it has been the only altimeter mission that has allowed a global assessment of local water surface slopes prior to SWOT, albeit with a 91 day orbit repeat cycle (Scherer et al., 2022, 2023).

With PICTA, we can explicitly derive not only the local slope of the river, but also its water level discontinuities around dams. To illustrate this, we provide four examples of barriers along the Creuse river in Fig. 7, right-hand side. Note that the river segments shown have been rotated for better visualization. The locations along the river are indicated by diamonds in the map (left). We show here the PICTA-derived river water level measurements at 10 m resolution, but without median filtering. Therefore, some outliers are remaining. However, the abrupt changes in water level of meter-magnitude caused by the dams are clearly visible in all cases, when compared to the underlying satellite imagery. In cases III and IV the measured level change is not perfectly coincident with the locations of the dams, due to their rotated orientation with respect to the satellite cross-track direction.

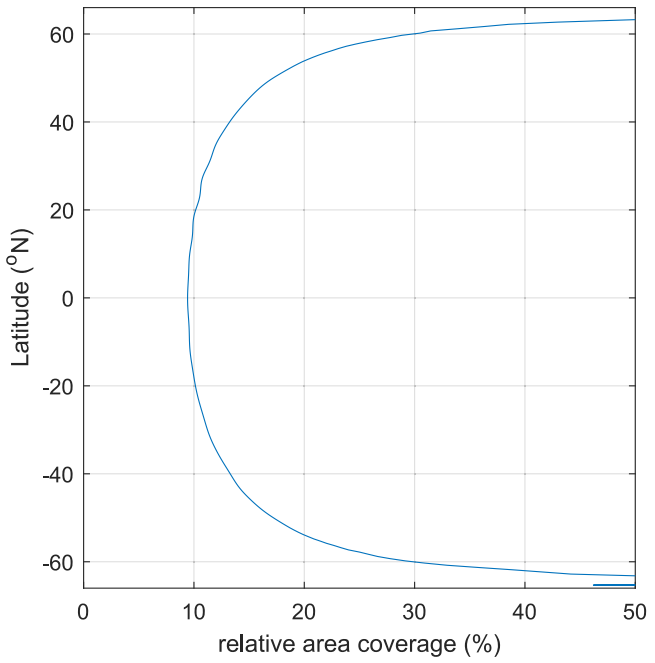

Fig. 10. Estimate of Sentinel-6 global area coverage over Latitude (no land mask applied) when assuming a swath of 14 km width in cross-track direction. The average relative coverage between −66°–66° Latitude is 17 %, meaning that this much of the Earth's water bodies may potentially be monitored with the Sentinel-6 A satellite. If the downlinked data was not truncated (onboard RMC mode desactivated), the potential coverage could almost double.

5. Limitations and outlook

The Sentinel-6 mission provides continuity for the previous reference series of altimetry missions, Europe & USA's Jason series. It is following an orbit with a 10 day repeat cycle at the cost of an inter-track distance of about 300 km at the equator. This means, spatial coverage is limited when compared, e.g., to the Sentinel-3 mission with 52 km inter-track distance (owing to its 27 days orbit repeat cycle and two satellites in interleaved orbit). Nevertheless, we want to estimate the theoretically possible coverage of the PICTA method for river profile retrieval developed here. Assuming a 14 km wide swath, meaning a maximum cross-track distance of 7 km with respect to the ground track, we can estimate the global area coverage achieved with the Sentinel-6 reference orbit, see Fig. 10. The average area coverage in the range of −66–66 degrees latitude is 17 %, meaning that the off-nadir processing may potentially enable us to gain a significant additional amount of water level measurements globally. For now, the upper limit for the swath width is enforced mainly by the RMC mode operation onboard the Sentinel-6 satellite, in which half the recorded signal (the waveform tails) are effectively deleted with the goal to reduce the amount of data to be transferred to the ground. While this has virtually no consequences for the quality of ocean measurements, it drastically limits the global coverage for novel hydrologic applications such as presented here. The estimated coverage could almost be doubled if the downlinked data was not truncated. A proper quantification of the information gain compared to the classical along-track observations is difficult for several reasons. Firstly, the classical altimeter observations are located along the ground track lines, which — mathematically speaking — cover zero area. Secondly, if we attempted to estimate the gain based on the number of available observations instead, already a comparison of along-track FFSAR products versus unfocused SAR products would be hampered by the different resolutions and noise levels, not to mention that an actual assessment of the number of observations gained from the off-nadir PICTA approach would require global processing of a detailed database of rivers and lakes in combination with the satellite tracks and the altimeter's tracker range setting.

Yet, we need to stress that the coverage estimate should be considered a theoretical upper margin, since there will be too complex or too dynamic scenes in which water targets cannot be distinguished (left–right ambiguity) or show poor contrast with the environment due to varying water surface roughness, varying incidence angles or the presence of too many bright scatterers. A general limitation is the orientation of the river with respect to the ground track, i.e. only a handful of measurements may be available for a river oriented in cross-track direction. The inclination of the Sentinel-6 mission is 66 degrees (Donlon et al., 2021), making PICTA more favorable for rivers oriented north-south than for rivers oriented east–west. Another main limitation of the method is the folding of the signal, as left and right are indistinguishable in the range coordinate, see Fig. 11 (and also Kleinherenbrink et al., 2020b; Altiparmaki et al., 2022). For illustration, according to Eq. (9) a scatterer at cross-track distance x and altitude H can be found at range gate

$$r = \frac{H_s - R_{\text{trk}} - H + Kx^2}{\delta r} + r_{\text{ref}}, \tag{23}$$

but a scatterer at $-x$ is equally mapped onto the same range gate. However, PICTA would still be applicable if

1. the backscatter from the opposite scatterer was much lower or
2. if there was no second scatterer at the opposite cross-track location to start with or
3. if the opposite scatterer was located at a sufficiently different altitude H ($\Delta H >$ several δr).

A proper estimate of the applicability and coverage of PICTA would therefore require the a-priori knowledge of locations and altitudes (water levels) of all targets in the footprint, which is typically unavailable — otherwise altimeter measurements would be obsolete. Yet, following the above-listed scenarios, PICTA is expected to be most applicable to scenes with

1. few *versus* many targets,
2. an undulating *versus* a flat topography,
3. rivers oriented approximately north-south *versus* rivers oriented east–west.

To elaborate on the aforementioned limitations, we discuss two specific scenes in Fig. 11 hereafter.

The left-hand side of Fig. 11 shows the outline of the Lek river in the Netherlands and the corresponding FFSAR signals recorded at two different times. In the first radargram, the signal from the river is clearly visible, although it is partly overshadowed by another strong signal located around range sample 150. This signal originates from the dense network of ditches in the polders around Kinderdijk, which produce an almost ocean-like echo on top of the river's signal. The water level in the polders is lower than that of the river, which we can confirm by looking at the echoes close to nadir, around 3–5 km. Inspecting the second radargram, the river is not visible, except for a few short segments close to nadir. This is probably caused by varying backscatter coefficients of both the river and the ditches, due to wind effects and altered mean squared slopes of the water surfaces. The cases shown are extremes of high and low contrast, typically an in-between state with partial visibility of river segments occurs in the period from 2021–2022. While the river water level can be measured in the first case, it is not possible in the second case due to lack of contrast. Hence, the number of available measurements depends not only on swath coverage but also on the environmental conditions.

The second case shows the FFSAR signal of the Sognefjord in the South of Norway, see right-hand side of Fig. 11. Again, left and right sides cannot be distinguished in the range samples, so the signals from both sides are folded. We observe that the return signal is typically strongest in the branches of the fjord and towards some of the shores,

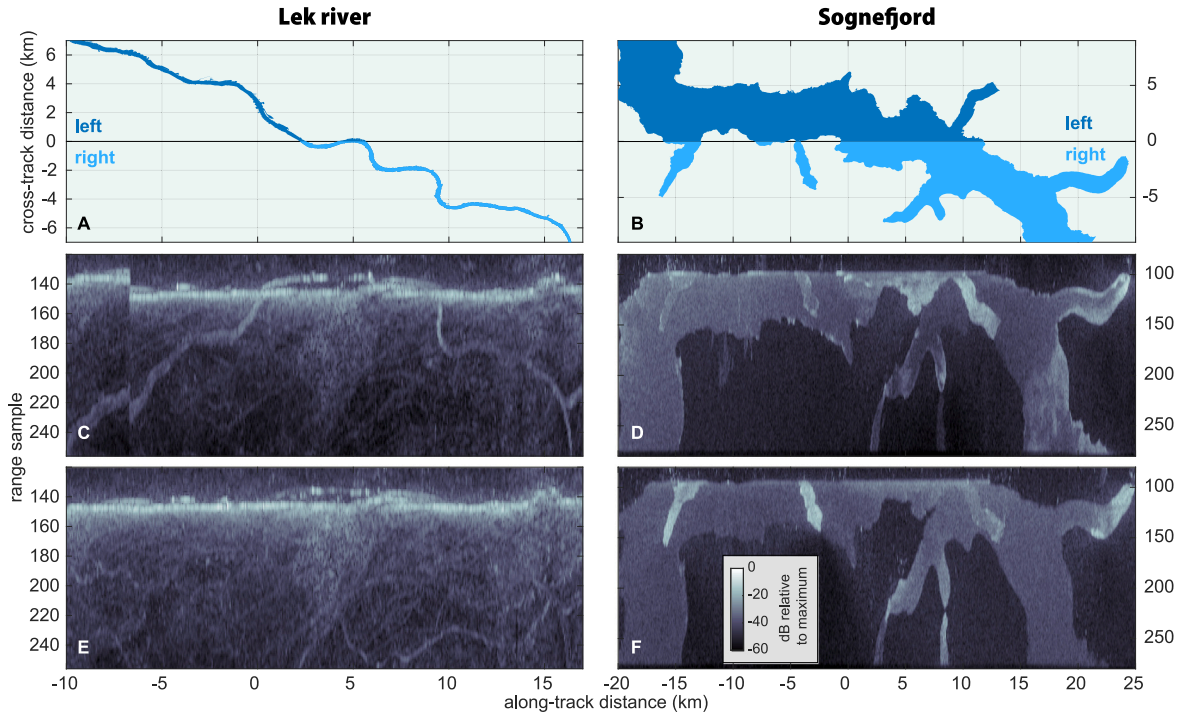

Fig. 11. Illustration of two scenes, which would challenge the current PICTA algorithm implementation. For each scene we provide the FFSAR signal of two overpasses. Note that the signal is folded, as the range coordinate cannot distinguish left and right. The Lek river signal (left-hand side) is not always visible. It is partly to completely overshadowed by a dense irrigation network of ditches, causing an almost ocean-like return echo around range sample 150. The return signals of the Sognefjord show greatly varying backscatter over different parts of the water surface and at different instances in time, particularly in its branches, challenging the current threshold retracking method.

presumably due to calmer surface states, for example due to less wind-driven waves (shorter fetch) and a reduced mean squared slope, resulting in a more specular echo from those surface facets. It should be emphasized that the water return signals differ spatially by orders of magnitude. We notice as well, that while some of the fjord's branches are very bright in one case, they may appear much less accentuated to almost invisible in the other. Technically, an algorithm similar to the one developed here can be applied to infer water level along the shores, however, the target's extent poses some challenges due to the varying backscatter, surface state and mean squared slope. In the case of narrow rivers or small lakes there are no pronounced differences between the surface state at both shores, since their surface generally remains calm compared to oceans and large lakes, hence an averaging over both shores can remove potential retracker biases as suggested in this work. For extended targets such as a fjord this assumption breaks down, so a physics-based numerical retracker such as in Boy et al. (2022) could be beneficial. However, the two-dimensional maps of surface state, backscatter and mean squared slope are generally unknown, requiring a potential numerical retracker to infer these (or mimic their effect at the very least) simultaneously to the water level. It is uncertain whether a numerical model can be designed to simultaneously describe and robustly invert such a variety of different scenarios in a practical way. Generally, due to the spatial variability of the surface conditions, we suppose that it is in any case beneficial to model the trailing and leading edges separately instead of the full waveforms, which is in line with the philosophy of a handful of existing retrackers, take for example the validated ALES retracker (Passaro et al., 2014). Also, as shown in this work in Section 2.2, it is strongly advisable to consider the return signal as a 2D image prior to retracking, in order to first determine which part of the signal corresponds to which feature on ground. We have not shown it here specifically, but without this step any off-the-shelf retrackers that provide a single range estimate per waveform are inherently incapable of reliably handling meanders with several echos per waveform (see Fig. 3) or bifurcations (see the Creuse river in Figs. 6 and 7).

6. Conclusion

In this work, we present a proof of concept of a semi-automated PICTA algorithm allowing to retrieve river water level profiles from the Sentinel-6 nadir altimeter data. Instead of obtaining only point measurements over Virtual Stations (VS), the PICTA method allows us to obtain river water level at 10 m along-track resolution, with an accuracy better than a decimeter, and within an approximately 14 km wide swath centered around the satellite's ground track (depending on topography, clutter and instrument operation mode). Even rivers with no or few nadir crossings (VS) can potentially be monitored with great detail, provided they are visible within the recorded range window. From the high-resolution profiles, water level discontinuities can be identified and local surface slopes are calculated with ease. Particularly encouraging is that the presented PICTA method boosts the potential coverage of Sentinel-6 A to about 17% of the land area between −66–66 degrees latitude on the one hand, and can potentially be generalized to any water body whose contours are visible within the footprint on the other hand, e.g. lakes and coasts. With that in mind, the globally available Sentinel-6 river water level measurements can be increased by orders of magnitude — solely by altered data processing.

Since the type of observation, and their respective accuracies and precisions are well within the mission goal margins of the recently launched SWOT mission, the Sentinel-6 data could eventually be processed in very similar way to produce emulated SWOT mission products such as discharge (Durand et al., 2023). Such a combined dataset offers unique opportunities for cross-calibration, as SWOT relies on interferometry, and serves to double the temporal sampling rate over the areas covered by Sentinel-6, ultimately benefitting all hydrological applications and science objectives. It should be emphasized that this requires reprocessing of all Sentinel-6 data acquired over land using fully focused SAR (Egido and Smith, 2017; Guccione et al., 2018) in the first place, which we strongly recommend in view of the new opportunities.

CRediT authorship contribution statement

Frithjof Ehlers: Writing – review & editing, Writing – original draft, Visualization, Validation, Software, Methodology, Investigation, Formal analysis, Data curation, Conceptualization. **Cornelis Slobbe:** Writing – review & editing, Supervision, Software, Project administration, Funding acquisition. **Florian Schlembach:** Writing – review & editing, Software. **Marcel Kleinherenbrink:** Writing – review & editing, Software, Methodology. **Martin Verlaan:** Writing – review & editing, Supervision, Project administration, Funding acquisition.

Declaration of competing interest

The authors declare the following financial interests/personal relationships which may be considered as potential competing interests: Frithjof Ehlers reports financial support was provided by Dutch Research Council. If there are other authors, they declare that they have no known competing financial interests or personal relationships that could have appeared to influence the work reported in this paper.

Acknowledgments

This research was supported by the Nederlandse Organisatie voor Wetenschappelijk Onderzoek (NWO) under grant no. ALWGO.2019.016. We thank the HydroPortail and EUMETSAT Data Store services for providing the in-situ and radar altimetry data, respectively, which fascilitated this research. We also thank the three anonymous reviewers for their curiosity, their effort and their detailed feedback, which helped making this manuscript as comprehensible as possible.

We want to warmly acknowledge the efforts of Francois Boy (CNES, France). Not only did he courteously contribute the airborne vorteX.io data to our analysis, but openly shared his own complementary experiences and knowledge with us.

Appendix A. Approximate geometry

We claimed that H was on the order of 100 m. To be precise, 100 m is the approximate size of the altimeter's range window, over which the return signal is recorded. This means, we implicitly assumed in Eqs. (2)–(4)—without loss of generality — that the tracker range was equal to the satellite altitude for brevity. If the tracker range was different or H was indeed much larger than 100 m, i.e., in a mountainous area, we would simply shift the origin in Fig. 2 to the surface height assumed by the onboard tracker $H_{\text{tracker}} = H_s - R_{\text{tracker}}$ via the replacement $H \to H - H_{\text{tracker}}$ and $R_E \to R_E + H_{\text{tracker}}$ in Eqs. (2)–(4). That said, the coordinate system can always be chosen such that H is at most 100 m, so the assumption stays valid. We can use the small angle approximation $\varphi \approx x/R_E$ in combination with the Taylor series expansion of cosine and sine functions and approximate Eqs. (3) and (4) to

$$y \approx (H + R_E)\left(1 - \frac{\varphi^2}{2}\right) - R_E$$
$$= H - R_E\frac{\varphi^2}{2} - \cancel{H\frac{\varphi^2}{2}} \tag{A.1}$$

and

$$x = (R_E + H)\sin\varphi \approx R_E\varphi + \cancel{H\varphi}. \tag{A.2}$$

The first omitted term is on the order of ∼0.1 mm, which is negligible compared to the altimeter ranging accuracy. The second omitted term is on the order of ∼10 cm, which is negligible compared to the mapping precision of river bank locations, considering e.g. changes over time.

In a next step we simplify Eq. (2) to calculate the height y in the Cartesian coordinates. We can rewrite it to

$$R = \sqrt{(H_s - y)^2 + x^2} = (H_s - y)\sqrt{1 + \frac{x^2}{(H_s - y)^2}}, \tag{A.3}$$

and use the Taylor expansion of $\sqrt{1+\varepsilon} \approx 1 + \varepsilon/2$ to obtain

$$y \approx H_s - R + \frac{x^2}{2H_s} \tag{A.4}$$

Hence, once the cross-track distance x and the measured range R of the river bank are obtained from the river polygon and the altimeter data, we can subsequently calculate the river water surface elevation H using Eqs. (A.1), (A.2) and (A.4), which yields

$$H = H_s - R + \frac{x^2}{2H_s} + \frac{x^2}{2R_E} = H_s - R + Kx^2, \tag{A.5}$$

with $K = (2H_s)^{-1} + (2R_E)^{-1}$. The systematic error made by using Eq. (5) instead of Eqs. (2)–(4) is maximally 1.2 mm up to cross-track distances of 7 km and with Sentinel-6 orbit parameters. This error can be corrected with a look-up-table if deemed necessary.

Appendix B. Threshold choice

Our choice of the threshold is motivated by the expected speckle noise level after averaging of 10 along-track resolution cells. Let us elaborate this with the following numerical experiment: It is well-established that the intensity (equivalently power) in a SAR image — the FFSAR radargram is nothing else — is Gamma distributed, with shape parameter equal to the number of independent looks (Intajag and Sukkasem, 2009, and references therein), namely ∼10 in this case. Suppose a river segment of constant intensity extends over 10 range resolution cells (equivalent to ∼24 range gates for Sentinel-6 data zero-padded to 512 range gates), then we can model this signal as a series of 10 random samples from the same Gamma distribution. After normalization with the maximum and right before thresholding, we require all 10 random samples to remain above the threshold value, since otherwise the retracking will detect only parts of the river signal and effectively fail to provide reasonable ranges. The chance for failure is ∼25% for the common threshold value of 0.5, ∼10% for 0.4, but smaller than 0.2% for a threshold below 0.2. Since the assumptions are idealized, we set a threshold of 0.1. In general, the applied threshold must be traded off against the along-track averaging on the one hand and the contrast of the river signal in the radargram on the other.

Data and code availability

The underlying FFSAR-processed Sentinel-6 altimetry signal and the corresponding PICTA-derived river water level profiles of the Garonne and Creuse rivers can be obtained from the 4TU repository *Research data underlying "Polygon-Informed Cross-Track Altimetry (PICTA): Estimating river water level profiles with the Sentinel-6 altimeter"* (DOI: https://doi.org/10.4121/304db898-f99c-490a-97c4-13f919ae3c05).

The source code of the scripts for PICTA-processing is made available via the github repository *Polygon-informed-cross-track-altimetry-PICTA* (URL: https://github.com/fehlers94/Polygon-informed-cross-track-altimetry-PICTA/tree/v1.0, DOI: https://doi.org/10.5281/zenodo.13165945).

References

Alsdorf, D.E., Lettenmaier, D.P., 2003. Tracking fresh water from space. Science 301 (5639), 1491–1494. http://dx.doi.org/10.1126/science.1089802, URL: https://www.science.org/doi/10.1126/science.1089802, Publisher: American Association for the Advancement of Science.

Altenau, E.H., Pavelsky, T.M., Durand, M.T., Yang, X., Frasson, R.P.d., Bendezu, L., 2021. The surface water and ocean topography (SWOT) mission river database (SWORD): A global river network for satellite data products. Water Resour. Res. 57 (7), e2021WR030054. http://dx.doi.org/10.1029/2021WR030054, URL: https://onlinelibrary.wiley.com/doi/abs/10.1029/2021WR030054.

Altiparmaki, O., Kleinherenbrink, M., Naeije, M., Slobbe, C., Visser, P., 2022. SAR altimetry data as a new source for swell monitoring. Geophys. Res. Lett. 49 (7), e2021GL096224. http://dx.doi.org/10.1029/2021GL096224, URL: https://onlinelibrary.wiley.com/doi/abs/10.1029/2021GL096224.

Belloni, R., Camici, S., Tarpanelli, A., 2021. Towards the continuous monitoring of the extreme events through satellite radar altimetry observations. J. Hydrol. 603, 126870. http://dx.doi.org/10.1016/j.jhydrol.2021.126870, URL: https://www.sciencedirect.com/science/article/pii/S0022169421009203.

Biancamaria, S., Lettenmaier, D.P., Pavelsky, T.M., 2016. The SWOT mission and its capabilities for land hydrology. In: Cazenave, A., Champollion, N., Benveniste, J., Chen, J. (Eds.), Remote Sensing and Water Resources. Springer International Publishing, Cham, pp. 117–147. http://dx.doi.org/10.1007/978-3-319-32449-4_6.

Birkett, C.M., 1998. Contribution of the TOPEX NASA radar altimeter to the global monitoring of large rivers and wetlands. Water Resour. Res. 34 (5), 1223–1239, arXiv:https://agupubs-onlinelibrary-wiley-com.tudelft.idm.oclc.org/doi/pdf/10.1029/98WR00124 URL: https://agupubs-onlinelibrary-wiley-com.tudelft.idm.oclc.org/doi/abs/10.1029/98WR00124 doi: https://doi-org.tudelft.idm.oclc.org/10.1029/98WR00124.

Birkett, C., Reynolds, C., Beckley, B., Doorn, B., 2011. From research to operations: The USda global reservoir and lake monitor. In: Vignudelli, S., Kostianoy, A.G., Cipollini, P., Benveniste, J. (Eds.), Coastal Altimetry. Springer Berlin Heidelberg, Berlin, Heidelberg, pp. 19–50. http://dx.doi.org/10.1007/978-3-642-12796-0_2.

Birkinshaw, S.J., Moore, P., Kilsby, C., O'Donnell, G.M., Hardy, A., Berry, P.a.M., 2014. Daily discharge estimation at ungauged river sites using remote sensing. Hydrol. Process. 28 (3), 1043–1054. http://dx.doi.org/10.1002/hyp.9647, URL: https://onlinelibrary.wiley.com/doi/abs/10.1002/hyp.9647.

Boergens, E., Buhl, S., Dettmering, D., Klüppelberg, C., Seitz, F., 2017. Combination of multi-mission altimetry data along the Mekong River with spatio-temporal kriging. J. Geod. 91 (5), 519–534. http://dx.doi.org/10.1007/s00190-016-0980-z.

Boy, F., Crétaux, J.-F., Boussaroque, M., Tison, C., 2022. Improving sentinel-3 SAR mode processing over lake using numerical simulations. IEEE Trans. Geosci. Remote Sens. 60, 1–18. http://dx.doi.org/10.1109/TGRS.2021.3137034, URL: https://ieeexplore.ieee.org/document/9656730, Conference Name: IEEE Transactions on Geoscience and Remote Sensing.

Boy, F., Poisson, J.-C., Fouqueau, V., Picot, N., Le Gac, S., 2023. Measuring longitudinal river profiles from sentinel-6 fully-focused SAR mode. In: 2023 Ocean Surface Topography Science Team (OSTST) Meeting. http://dx.doi.org/10.24400/527896/a03-2023.3781.

Calmant, S., da Silva, J.S., Moreira, D.M., Seyler, F., Shum, C.K., Crétaux, J.F., Gabalda, G., 2013. Detection of envisat RA2/ICE-1 retracked radar altimetry bias over the amazon basin rivers using GPS. Adv. Space Res. 51 (8), 1551–1564. http://dx.doi.org/10.1016/j.asr.2012.07.033, URL: https://www.sciencedirect.com/science/article/pii/S0273117712005091.

Copernicus, 2024. Copernicus global land services, URL: https://land.copernicus.eu/global/products/wl.

Crétaux, J.-F., Arsen, A., Calmant, S., Kouraev, A., Vuglinski, V., Bergé-Nguyen, M., Gennero, M.-C., Nino, F., Abarca Del Rio, R., Cazenave, A., Maisongrande, P., 2011. SOLS: A lake database to monitor in the Near Real Time water level and storage variations from remote sensing data. Adv. Space Res. 47 (9), 1497–1507. http://dx.doi.org/10.1016/j.asr.2011.01.004, URL: https://www.sciencedirect.com/science/article/pii/S0273117711000287.

Crétaux, J., Abarca-del Rio, R., Bergé-Nguyen, M., Arsen, A., Drolon, V., Clos, G., Maisongrande, P., 2016. Lake volume monitoring from space. Surv. Geophys. 37, http://dx.doi.org/10.1007/s10712-016-9362-6.

Daguzé, J.A., Calassou, G., Le Gac, S., Boy, F., 2023. Using image processing techniques to detect inland water bodies in Sentinel-6MF Fully Focused SAR radargrams and improve water surface height retrieval: A case study over garonne river. In: 2023 Ocean Surface Topography Science Team (OSTST) Meeting. http://dx.doi.org/10.24400/527896/a03-2023.3801.

Dibarboure, G., Labroue, S., Ablain, M., Fjortoft, R., Mallet, A., Lambin, J., Souyris, J.-C., 2012. Empirical cross-calibration of coherent SWOT errors using external references and the altimetry constellation. IEEE Trans. Geosci. Remote Sens. 50 (6), 2325–2344. http://dx.doi.org/10.1109/TGRS.2011.2171976, URL: https://ieeexplore.ieee.org/abstract/document/6087373.

Dibarboure, G., Ubelmann, C., Flamant, B., Briol, F., Peral, E., Bracher, G., Vergara, O., Faugère, Y., Soulat, F., Picot, N., 2022. Data-driven calibration algorithm and pre-launch performance simulations for the SWOT mission. Remote Sens. 14 (23), 6070. http://dx.doi.org/10.3390/rs14236070, URL: https://www.mdpi.com/2072-4292/14/23/6070, Number: 23 Publisher: Multidisciplinary Digital Publishing Institute.

Dinardo, S., 2020. Techniques and Applications for Satellite SAR Altimetry over Water, Land and Ice (Ph.D. thesis). Technische Universität, Darmstadt, URL: https://tuprints.ulb.tu-darmstadt.de/11343/. ISBN: 9783935631457 Volume: 56.

Donlon, C.J., Cullen, R., Giulicchi, L., Vuilleumier, P., Francis, C.R., Kuschnerus, M., Simpson, W., Bouridah, A., Caleno, M., Bertoni, R., Rancaño, J., Pourier, E., Hyslop, A., Mulcahy, J., Knockaert, R., Hunter, C., Webb, A., Fornari, M., Vaze, P., Brown, S., Willis, J., Desai, S., Desjonqueres, J.-D., Scharroo, R., Martin-Puig, C., Leuliette, E., Egido, A., Smith, W.H.F., Bonnefond, P., Le Gac, S., Picot, N., Tavernier, G., 2021. The Copernicus sentinel-6 mission: Enhanced continuity of satellite sea level measurements from space. Remote Sens. Environ. 258, 112395. http://dx.doi.org/10.1016/j.rse.2021.112395, URL: https://www.sciencedirect.com/science/article/pii/S0034425721001139.

Durand, M., Gleason, C.J., Pavelsky, T.M., Prata de Moraes Frasson, R., Turmon, M., David, C.H., Altenau, E.H., Tebaldi, N., Larnier, K., Monnier, J., Malaterre, P.O., Oubanas, H., Allen, G.H., Astifan, B., Brinkerhoff, C., Bates, P.D., Bjerklie, D., Coss, S., Dudley, R., Fenoglio, L., Garambois, P.-A., Getirana, A., Lin, P., Margulis, S.A., Matte, P., Minear, J.T., Muhebwa, A., Pan, M., Peters, D., Riggs, R., Sikder, M.S., Simmons, T., Stuurman, C., Taneja, J., Tarpanelli, A., Schulze, K., Tourian, M.J., Wang, J., 2023. A framework for estimating global river discharge from the surface water and ocean topography satellite mission. Water Resour. Res. 59 (4), e2021WR031614. http://dx.doi.org/10.1029/2021WR031614, URL: https://onlinelibrary.wiley.com/doi/abs/10.1029/2021WR031614.

Egido, A., Smith, W.H.F., 2017. Fully focused SAR altimetry: Theory and applications. IEEE Trans. Geosci. Remote Sens. 55 (1), 392–406. http://dx.doi.org/10.1109/TGRS.2016.2607122.

Ehlers, F., Schlembach, F., Kleinherenbrink, M., Slobbe, C., 2022. Validity assessment of SAMOSA retracking for fully-focused SAR altimeter waveforms. Adv. Space Res. http://dx.doi.org/10.1016/j.asr.2022.11.034, URL: https://www.sciencedirect.com/science/article/pii/S0273117722010651.

Ehlers, F., Slobbe, C., Verlaan, M., Kleinherenbrink, M., 2023. A noise autocovariance model for SAR altimeter measurements with implications for optimal sampling. Adv. Space Res. 71 (10), 3951–3967. http://dx.doi.org/10.1016/j.asr.2023.02.043, URL: https://linkinghub.elsevier.com/retrieve/pii/S0273117723001734.

EUMETSAT, 2021. Sentinel-6/Jason-CS ALT level 1 product generation specification (L1 ALT PGS) | EUMETSAT. URL: https://www-cdn.eumetsat.int/files/.

Fouqueau, V., Poisson, J., Valladeau, G., Boy, F., Tourain, C., Tison, C., 2022. Development of a new UAV-based LiDAR altimetry solution for in-situ wave spectrum estimation. In: 2022 Ocean Surface Topography Science Team (OSTST) Meeting.

Fu, L.-L., Pavelsky, T., Cretaux, J.-F., Morrow, R., Farrar, J.T., Vaze, P., Sengenes, P., Vinogradova-Shiffer, N., Sylvestre-Baron, A., Picot, N., Dibarboure, G., 2024. The surface water and ocean topography mission: A breakthrough in radar remote sensing of the ocean and land surface water. Geophys. Res. Lett. 51 (4), e2023GL107652. http://dx.doi.org/10.1029/2023GL107652, URL: https://onlinelibrary.wiley.com/doi/abs/10.1029/2023GL107652.

Guccione, P., Scagliola, M., Giudici, D., 2018. 2D frequency domain fully focused SAR processing for high PRF radar altimeters. Remote Sens. 10 (12), 1943. http://dx.doi.org/10.3390/rs10121943, URL: https://www.mdpi.com/2072-4292/10/12/1943, Number: 12 Publisher: Multidisciplinary Digital Publishing Institute.

Gustafsson, D., Andersson, J., Brito, F., Martinez, B., Arheimer, B., 2018. New tool to share data and models in hydrological forecasting, based on the ESA TEP. In: EGU General Assembly Conference Abstracts. In: EGU General Assembly Conference Abstracts, p. 18723.

Halicki, M., Schwatke, C., Niedzielski, T., 2023. The impact of the satellite ground track shift on the accuracy of altimetric measurements on rivers: A case study of the Sentinel-3 altimetry on the Odra/Oder River. J. Hydrol. 617, 128761. http://dx.doi.org/10.1016/j.jhydrol.2022.128761, URL: https://www.sciencedirect.com/science/article/pii/S0022169422013312.

Intajag, S., Sukkasem, N., 2009. Speckle filtering by generalized Gamma distribution. In: 2009 Fifth International Joint Conference on INC, IMS and IDC. pp. 1335–1338. http://dx.doi.org/10.1109/NCM.2009.262, URL: https://ieeexplore.ieee.org/document/5331457.

Kleinherenbrink, M., Naeije, M., Slobbe, C., Egido, A., Smith, W., 2020a. The performance of CryoSat-2 fully-focussed SAR for inland water-level estimation. Remote Sens. Environ. 237, 111589. http://dx.doi.org/10.1016/j.rse.2019.111589, URL: https://linkinghub.elsevier.com/retrieve/pii/S0034425719306091.

Kleinherenbrink, M., Smith, W.H., Naeije, M.C., Slobbe, D.C., Hoogeboom, P., 2020b. The second-order effect of Earth's rotation on Cryosat-2 fully focused SAR processing. J. Geod. 94 (1), http://dx.doi.org/10.1007/s00190-019-01337-8, URL: http://www.scopus.com/inward/record.url?scp=85077329577&partnerID=8YFLogxK.

Lagarias, J.C., Reeds, J.A., Wright, M.H., Wright, P.E., 1998. Convergence properties of the Nelder–Mead Simplex Method in low dimensions. SIAM J. Optim. 9 (1), 112–147. http://dx.doi.org/10.1137/S1052623496303470, URL: https://epubs.siam.org/doi/10.1137/S1052623496303470, Publisher: Society for Industrial and Applied Mathematics.

Laxon, S., 1994. Sea ice altimeter processing scheme at the EODC. Int. J. Remote Sens. 15 (4), 915–924. http://dx.doi.org/10.1080/01431169408954124.

Nielsen, K., Zakharova, E., Tarpanelli, A., Andersen, O.B., Benveniste, J., 2022. River levels from multi mission altimetry, a statistical approach. Remote Sens. Environ. 270, 112876. http://dx.doi.org/10.1016/j.rse.2021.112876, URL: https://www.sciencedirect.com/science/article/pii/S0034425721005964.

Passaro, M., Cipollini, P., Vignudelli, S., Quartly, G.D., Snaith, H.M., 2014. ALES: A multi-mission adaptive subwaveform retracker for coastal and open ocean altimetry. Remote Sens. Environ. 145, 173–189. http://dx.doi.org/10.1016/j.rse.2014.02.008, URL: https://www.sciencedirect.com/science/article/pii/S0034425714000534.

Raney, R., 1998. The delay/Doppler radar altimeter. IEEE Trans. Geosci. Remote Sens. 36 (5), 1578–1588. http://dx.doi.org/10.1109/36.718861.

Raney, R., 2012. CryoSat SAR-mode looks revisited. IEEE Geosci. Remote Sens. Lett. 9 (3), 393–397. http://dx.doi.org/10.1109/LGRS.2011.2170052.

Scherer, D., Schwatke, C., Dettmering, D., Seitz, F., 2022. ICESat-2 based river surface slope and its impact on water level time series from satellite altimetry. Water Resour. Res. 58 (11), e2022WR032842. http://dx.doi.org/10.1029/2022WR032842, URL: https://onlinelibrary.wiley.com/doi/abs/10.1029/2022WR032842, _eprint: https://agupubs.onlinelibrary.wiley.com/doi/pdf/10.1029/2022WR032842.

Scherer, D., Schwatke, C., Dettmering, D., Seitz, F., 2023. ICESat-2 river surface slope (IRIS): A global reach-scale water surface slope dataset. Sci. Data 10 (1), 359. http://dx.doi.org/10.1038/s41597-023-02215-x, URL: https://www.nature.com/articles/s41597-023-02215-x, Publisher: Nature Publishing Group.

Schwatke, C., Dettmering, D., Bosch, W., Seitz, F., 2015. DAHITI – an innovative approach for estimating water level time series over inland waters using multi-mission satellite altimetry. Hydrol. Earth Syst. Sci. 19 (10), 4345–4364. http://dx.doi.org/10.5194/hess-19-4345-2015, URL: https://hess.copernicus.org/articles/19/4345/2015/.

Schwatke, C., Halicki, M., Scherer, D., 2023. Generation of High-Resolution Water Surface Slopes from Multi-Mission Satellite Altimetry. Preprint, Preprints, http://dx.doi.org/10.22541/essoar.167979550.06401677/v1, URL: https://www.authorea.com/users/473835/articles/631172-generation-of-high-resolution-water-surface-slopes-from-multi-mission-satellite-altimetry?commit=fbe7f28bd55b36862de2c5735dea6c44b8acc392.

Tourian, M.J., Schwatke, C., Sneeuw, N., 2017. River discharge estimation at daily resolution from satellite altimetry over an entire river basin. J. Hydrol. 546, 230–247. http://dx.doi.org/10.1016/j.jhydrol.2017.01.009, URL: https://www.sciencedirect.com/science/article/pii/S0022169417300100.

Tourian, M.J., Tarpanelli, A., Elmi, O., Qin, T., Brocca, L., Moramarco, T., Sneeuw, N., 2016. Spatiotemporal densification of river water level time series by multimission satellite altimetry. Water Resour. Res. 52 (2), 1140–1159. http://dx.doi.org/10.1002/2015WR017654, URL: https://onlinelibrary.wiley.com/doi/abs/10.1002/2015WR017654.

Villadsen, H., Deng, X., Andersen, O.B., Stenseng, L., Nielsen, K., Knudsen, P., 2016. Improved inland water levels from SAR altimetry using novel empirical and physical retrackers. J. Hydrol. 537, 234–247. http://dx.doi.org/10.1016/j.jhydrol.2016.03.051, URL: https://www.sciencedirect.com/science/article/pii/S0022169416301561.

Yanez, C., Boy, F., Calassou, G., Daguzé, J.-A., Asfour, K., 2024. Performance assessment of Lake Water Level estimation from Sentinel-6 Fully-Focused SAR observations and comparison to SWOT mission. Technical Report EGU24-5773, Copernicus Meetings, http://dx.doi.org/10.5194/egusphere-egu24-5773, URL: https://meetingorganizer.copernicus.org/EGU24/EGU24-5773.html, Conference Name: EGU24.